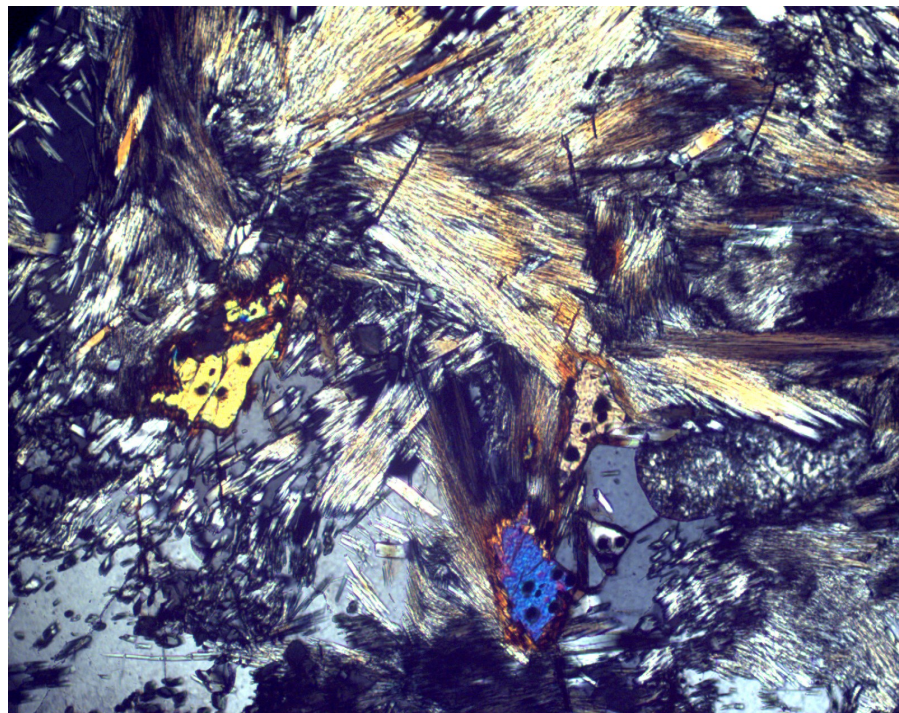# Metamorphic record of monazite in aluminous migmatitic gneisses at Stensjöstrand, Sveconorwegian orogen

Andreas Olsson

Dissertations in Geology at Lund University,
Master's thesis, no 467
(45 hp/ECTS credits)

Metamorphic record of monazite in aluminous migmatitic gneisses at Stensjöstrand, Sveconorwegian orogen

Master's thesis
Andreas Olsson

Department of Geology
Lund University
2016

Contents

Cover Picture: Monazite together with radiating sillimanite bundles in thin section. Photo by Andreas Olsson.

Metamorphic record of monazite in aluminous migmatitic gneisses at Stensjöstrand, Sveconorwegian orogen

ANDREAS OLSSON

Abstract: Laser Ablation Inductively Coupled Plasma Mass Spectrometry (LA-ICP-MS) has been utilised to investigate the age and chemical composition of two texturally different types of monazite in leucosome and mesosome of polymetamorphic aluminous migmatitic gneisses at Stensjöstrand, Halland. Results of radiometric dating are compared with previously published zircon dates. Monazite grains were documented and investigated in three thin sections using polarization microscopy and Scanning Electron Microscopy coupled with Energy Dispersive X-ray (SEM-EDX). Backscatter Electron (BSE) images show that monazite grains in the mesosome have anhedral morphology, embayments, and complex internal zonation. Monazite grains in the leucosome are relatively small, euhedral to subhedral or ovoid, and have relatively distinct internal zoning. Anhedral and ovoid morphologies, embayments, and complex zoning indicate recrystallisation and resorption processes having affected monazite grains during metamorphism. Documented monazite grains were analysed for trace elements Y, Lu, Th, and U, rare earth elements (REE), and radiometrically dated. Results reveal two age groups, c. 1.43 Ga and c. 0.99 Ga, that relate to the Hallandian and Sveconorwegian orogenies, respectively. Both monazite generations occur in leucosome and mesosome, either as single- or double-generation grains. Weighted average calculations of concordant $^{207}Pb/^{206}Pb$ isotopic dates yield 1434 ± 14 Ma and 988 ± 11 Ma, which can be compared to previously published zircon dates of 1386 ± 7 Ma and 970 ± 5 Ma (Piñán-Llamas et al. 2015). The analytical results may have been affected by data drift owing to downhole fractionation, most distinctly observed in results from Thompson Mine Monazite (TMM) standard as steadily increasing dates throughout the day of analysis. Trends in trace element analyses show relative U enrichment and depletion of Y, Lu, and Th in the 0.99 Ga monazite generation compared to the 1.43 Ga generation, indicating that the bulk of REE content in the rock may have been locked into the Hallandian generation preventing incorporation into the Sveconorwegian generation. In conclusion, obtained U-Pb monazite dates correlate broadly with U-Pb zircon dates, but are c. 50 Ma and c. 18 Ma older, for the Hallandian and Sveconorwegian generations, respectively.

Andreas Olsson, Department of Geology, Lund University, Sölvegatan 12, SE-223 62 Lund, Sweden.
E-mail: marcus.andreas.olsson@live.se

Metamorft avtryck i monazit i aluminös migmatitgnejs vid Stensjöstrand, Svekonorvegiska orogenesen

ANDREAS OLSSON

Sammanfattning: Laser Ablation Inductively Coupled Plasma Mass Spectrometry (LA-ICP-MS) har använts för att undersöka ålder och kemisk komposition av två texturellt skilda typer av monazit i leucosom och mesosom i polymetamorf aluminös migmatitgnejs vid Stensjöstrand, Halland. Dateringsresultat jämförs med tidigare publicerade zirkondateringar. Monazitkorn dokumenterades och undersöktes i tre tunnslip med hjälp av polarisationsmikroskopi och Scanning Electron Mikroskopy kopplat med Energy Dispersive X-ray (SEM-EDX). Backscatter Electron (BSE) bilder visar att monasitkorn i mesosomen har anhedral morfologi med inskärningar och komplex intern zonering. Monazitkorn i leucosomen är relativt små, euhedrala till subhedrala eller äggformiga och har relativt distinkt intern zonering. Anhedrala och äggformiga morfologier, inskärningar samt komplex zonering indikerar att monazitkornen har utsatts för omkristallations- och resorptionsprocesser vid metamorfism. Dokumenterade monazitkorn analyserades för spårelementen Y, Lu, Th och U, sällsynta jordartsmetaller (REE) samt utfördes ratdiometrisk datering. Dateringar visar två åldersgrupper, ca 1.43 Ga och ca 0.99 Ga, som relaterar till den Hallandiska respektive den Sveconorvegiska orogenesen. Båda generationer av monazit förekommer i leucosom samt mesosom, antingen som enstaka eller dubbelgenerations korn. Viktade medelvärdesberäkningar från konkordant $^{207}Pb/^{206}Pb$ isotopiska datum gav 1434 ± 14 Ma och 988 ± 11 Ma som kan jämföras med tidigare publicerade zirkondata, 1386 ± 7 Ma och 970 ± 5 Ma (Piñán-Llamas et al. 2015). De analytiska resultaten kan ha påverkats av datadrift på grund av s.k. downhole fractionation. Detta syns tydligast i resultat från standarden Thompson Mine Monazite (TMM) i form av stadigt ökande dateringar under dagen som analyserna genomfördes. Trender i spårelementanalyser visar relativ U anriktning samt utarmning av Y, Lu och Th i 0.99 Ga monazitgenerationen jämfört med 1.43 Ga generationen. Detta indikerar att bulkmängden av REE i bergarten kan ha blivit låst i den Hallandiska generationen vilket till följd har förhindrat inkorporering i den Svekonorvegiska generationen. Sammanfattningsvis korrelerar erhållna U-Pb monazitdateringar brett med U-Pb zirkondateringar, men är ca 50 Ma och ca 18 Ma äldre för Hallandiska respektive Svekonorvegiska generationer.

Andreas Olsson, Geologiska institutionen, Lunds Universitet, Sölvegatan 12, 223 62 Lund, Sverige.
E-post: marcus.andreas.olsson@live.se

1 Introduction

Eastern Segment is a metamorphic belt dominated by orthogneisses that extends over much of southwestern Sweden. It is the easternmost out of the five segments constituting the Sveconorwegian Province (Hansen et al. 2015). This metamorphic belt has been subject to two large-scale orogenies in the last c. 1500 Ma, namely the Hallandian and Sveconorwegian orogenies. These geological events are reflected in the rocks of the Eastern Segment, which are representative of deep orogenic genesis, having been metamorphosed at high P-T conditions and subsequently brought to the Earth's surface through erosion and tectonic exhumation.

Monazite is a rare earth phosphate mineral [LREE(PO$_4$)] occurring as an accessory phase. It has a variable composition that reflects conditions in the host rock. Monazite primarily accepts LREE (light rare earth elements: La-Eu) before HREE (heavy rare earth elements: Ga-Lu) into its crystal structure and also incorporates the radioactive elements U and Th. The presence of these radioactive elements, coupled with the fact that monazite incorporates only insignificant amounts of Pb, make this mineral viable as a geochronometer (Williams et al. 2007).

Monazite may harbour compositional domains, varying from simple to complex, which reflect periods of mineral growth. The chemical composition of a domain may be linked to the monazite forming reaction and the involved components. Knowing the constituents of such a reaction allows extrapolation of the physical conditions (pressure, temperature, and bulk chemical composition) of the host rock at the time the reaction took place. LA-ICP-MS can be used for analysis and dating of individual compositional domains, as small as 5 μm, resulting in a powerful dating tool.

This study examines two texturally differing types of monazite found in aluminous migmatitic gneisses at Stensjöstrand, Halland. One type consists of relatively large, partially resorbed and anhedral grains with complex zoning occurring in the mesosome whilst the other consists of smaller euhedral to subhedral rounded grains occurring in the leucosome. Multiple generations of monazite may be present as a result of the metamorphic events that have affected the study area. SEM and LA-ICP-MS have been used to conduct textural, compositional, and geochronological analysis of monazite in thin section ("in situ"). The aims of this study are to:

- Produce U-Th-Pb dates of monazite, in the same samples as dated by U-Pb zircon by Piñán-Llamas et al. (2015), and compare the zircon and monazite geochronology.
- Investigate the systematics in terms of texture, age, and chemical composition of monazite grains in mesosome and leucosome.
- Discuss whether or not monazite yields information different from that of zircon, and if that can give additional information on the metamorphic evolution of the Eastern Segment.

2 Background

2.1 Geological setting

The Sveconorwegian Province is situated in the southwestern part of the Baltic shield and is a tectonic counterpart to the Grenville orogen in North America (Bingen et al. 2008; Möller et al. 2015). This province is made up of five north to south trending metamorphic segments, in order from west to east; Telemarkia, Bamble, Kongsberg, Idefjorden and Eastern Segment (Fig. 1; Bingen et al. 2005).

Eastern Segment

The Eastern Segment hosts a metamorphic array across the frontal wedge in the east (greenschist-, amphibolite-facies) to the internal section in the west (upper amphibolite-, high pressure granulite-, and eclogite-facies; Möller et al. 2015). Previous studies have conducted geothermobarometry to achieve approximate temperatures and pressures from mafic rocks in the internal section. Results from the internal section were c. 680-800°C and c. 0.8-1.2 GPa with pressures >1.5 GPa in eclogite (Johansson et al. 1991; Wang & Lindh 1996; Möller 1998, 1999; Wang et al. 1998). The two main orogenies that have had an impact in the Eastern Segment are the Hallandian and Sveconorwegian orogenies dated to c. 1.47-1.38 Ga and c. 0.99-0.96 Ga respectively (overviews in Möller et al. 2015; Ulmius et al. 2015). The Hallandian is characterised by magmatism, migmatisation, and emplacement of granite and charnockite intrusives (Hubbard 1975, 1989; Christoffel et al. 1999; Söderlund et al. 2002; Möller et al. 2007; Brander et al. 2012; Ulmius et al. 2015). The Sveconorwegian event caused pervasive regional metamorphism and deformation of the Eastern Segment (Möller 1998, 1999; Andersson et al. 1999, 2002; Christoffel et al. 1999; Söderlund et al. 2002; Möller et al. 2007, 2015; Hansen et al. 2015; Piñán-Llamas et al. 2015; Tual et al. 2015).

Orthogneisses of granitic to quartz-monzonitic-granodioritic compositions are the main rock types in the Eastern Segment. These have protolith ages and chemical compositions similar to c. 1.7 Ga rocks of the Transscandinavian Igneous Belt (op. cit; Wahlgren et al. 1994; Petersson et al. 2013).

Regional geology

Stensjöstrands Naturreservat, also known as Naturreservat Steningekusten (Länsstyrelsen 2015), is a nature reserve located along the Swedish west coast in Halland County (Fig. 1). The focus of this study is sillimanite-bearing quartzofeldspathic migmatite gneiss (Fig. 2). Previous studies of this rock have yielded zircon dates of 1386 ± 7 Ma and 970 ± 5 Ma corresponding with the Hallandian and Sveconorwegian events, respectively (Piñán-Llamas et al. 2015).
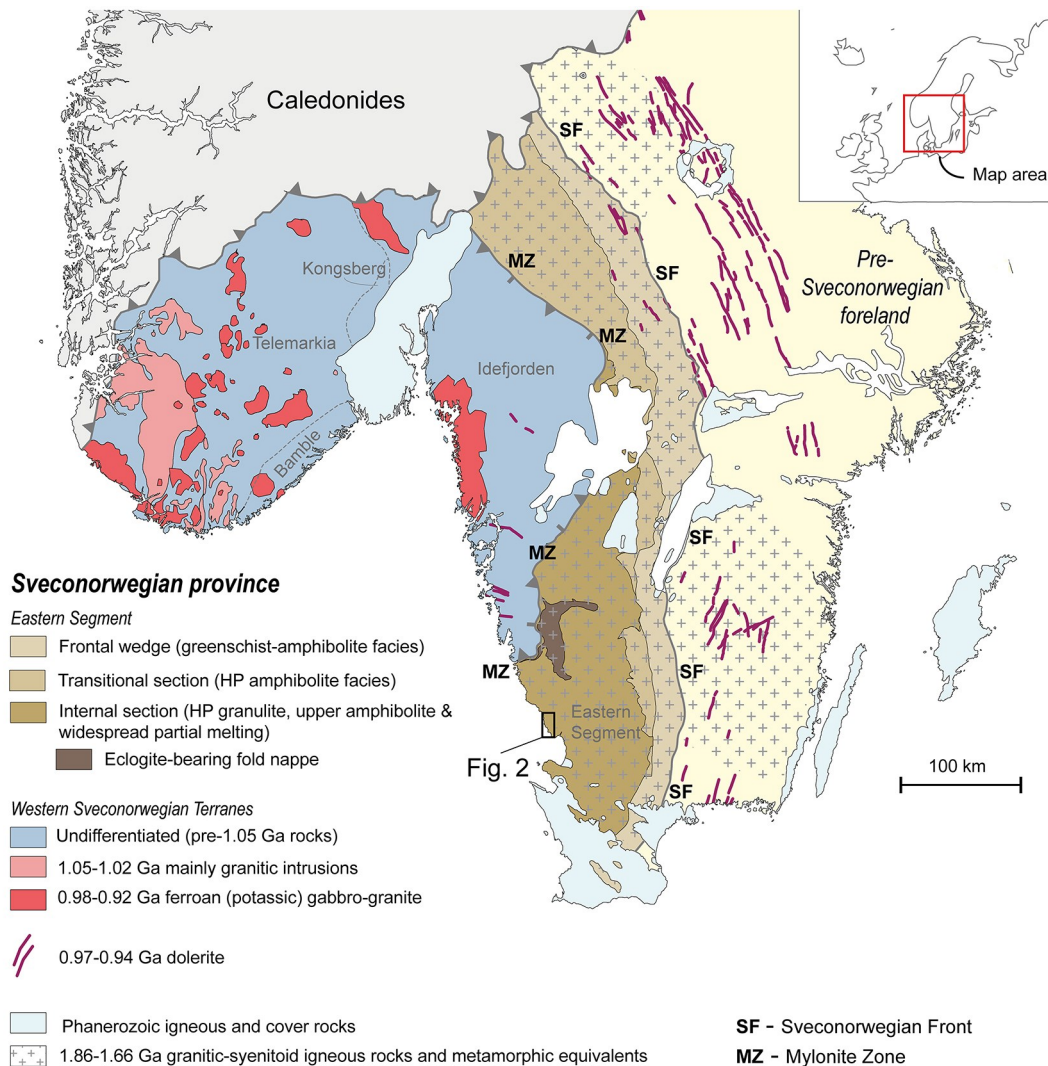
Fig. 1. Sketch map of the Sveconorwegian province in southern Sweden and Norway, showing the extent of the Eastern Segment (brown tones) and other terranes of the orogeny (bluish grey) located in the west (terrane divisions after Bingen et al., 2008; extent of Sveconorwegian magmatism in Telemarkia terrane after Slagstad et al., 2013). The black rectangle denotes the study area, Steninge. Figure based on 1:5 M Fennoscandian map database and Geological Survey of Sweden (SGU) 1:1 M Bedrock map database, compiled by Jenny Andersson, published in Piñán-Llamas et al., 2015. Reproduced with permission from Elsevier.

2.2 Monazite

Monazite is a phosphate mineral with the chemical formula (LREE)PO$_4$ that occurs as an accessory phase in many sedimentary, igneous and metamorphic rocks (Overstreet 1967). The mineral structure is built around PO$_4$ tetrahedra slightly offset in connection to nine-oxygen coordinated polyhedral (Williams et al. 2007). The polyhedron is irregular due to its vectors being of unequal length, making monazite part of the monoclinic crystal system (Williams et al. 2007). The nine-oxygen polyhedron is also the reason of monazite's relatively wide compositional variability (compared to other orthophosphate minerals such as xenotime; Beall et al. 1981; Williams et al. 2007). This compositional variability is particularly reflected by compositional zoning, also known as compositional domains. Compositional domains occasionally have distinct boundaries that can easily be identified in

back-scatter electron (BSE) images.

Igneous occurrences of monazite vary depending on rock composition. The mineral is most common in rocks with low CaO content (such as peraluminous granitoids), less common in peralkaline rocks, and unreported in primary mafic lavas and plutons (Williams et al. 2007). Monazite appears in sedimentary rocks as a detrital mineral or in small amounts through precipitation during diagenesis (Williams et al. 2007). Detrital monazite is also known to comprise large parts of beach sands in some areas of the world (Spear & Pyle 2002).

The reaction representing the first appearance of monazite during prograde metamorphism is disputed, as it has been observed in rocks of several metamorphic grades, from greenschist facies and above (Spear & Pyle 2002). Allanite is known to be a precursor to metamorphic monazite through a mo-
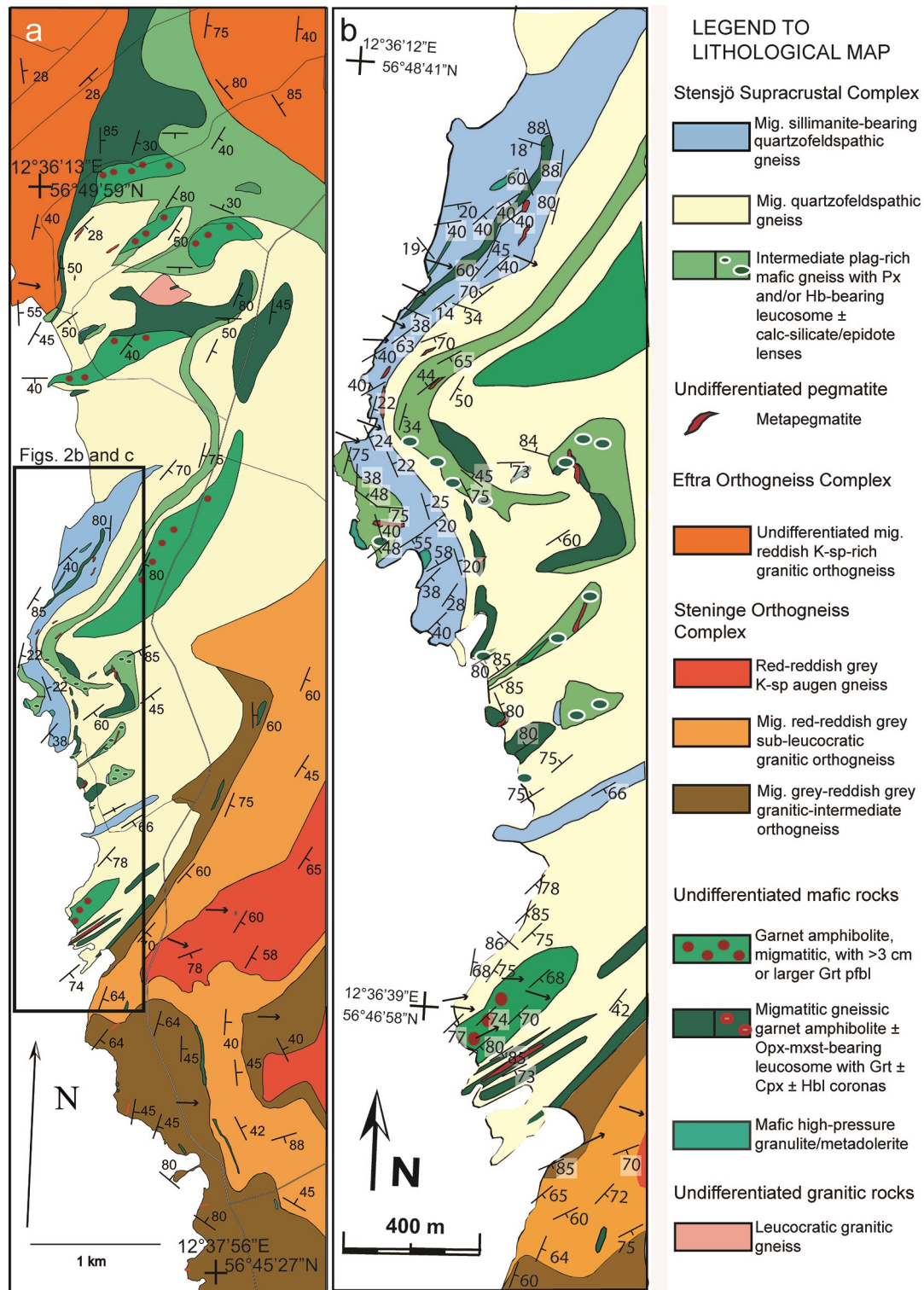
Fig. 2. Geological map of Steningekusten area along the Swedish west coast in Halland County. (a) Lithological map showing the different gneisses and the geologic structure of the study area. (b) Close up of the study area. The sillimanite-bearing quartzofeldspathic migmatite gneiss (bluish grey) is the main rock of interest in this study. Mapping performed by students from Hope College under supervision by Edward Hansen, Aranzazu Piñán-Llamas, and Leif Johansson, and by Charlotte Möller and Inger Lundqvist (SGU). Map compiled by Charlotte Möller, published in Piñán-Llamas et al., 2015. Reproduced with permission from Elsevier.

nazite-in reaction in the middle amphibolite-facies or the staurolite zone (Overstreet 1967; Smith & Barreiro 1990; Bingen et al. 1996; Mark Harrison et al. 1997; Rubatto et al. 2001; Wing et al. 2003). The size of a metamorphic monazite grain has in some studies (Rubatto et al. 2001) been correlated with metamorphic grade, i.e. larger crystals with increasing grade. The compositional domains of metamorphic monazite represent a certain reaction taking place in the rock (i.e. monazite producing reaction) that produced monazite either through the breakdown and redistribution of chemical components from other mineral and/or melt related phases (Williams et al. 2007), or through recrystallisation of pre-existing monazite.

The chemical composition of monazite depends on the physical conditions in the host rock. The nine-oxygen polyhedra in monazite's crystal structure favour the relatively large LREE (over smaller HREE) at its centre, although both types of REE elements (as well as [89]Y) are incorporated into the mineral (Williams et al. 2007). The trace element contents of monazite are particularly affected by the presence of garnet in the mineral assemblage (Spear & Pyle 2002). Both minerals act as sinks for [89]Y and HREE, meaning that the breakdown of one of these phases results in the release of these elements for the other (Williams et al. 2007). This implies that where monazite predates garnet formation the latter is likely to be depleted in [89]Y and HREE, and vice versa (Zhu & O'Nions 1999).

Along with REE and a number of other elements (most commonly Al, Ba, Ca, Pb, and Si), monazite incorporates the radioactive elements U and Th into its crystal structure, the former more so than the latter (Williams et al. 2007). The U-Th-Pb decay system ($^{235}U{\rightarrow}^{207}Pb$, $^{238}U{\rightarrow}^{206}Pb$, and $^{232}Th{\rightarrow}^{208}Pb$) in monazite can be utilised for geochronology largely because naturally occurring Pb (^{204}Pb) is incorporated only in negligible amounts and so virtually all Pb found in monazite is radiogenic (Faure & Mensing 2005).

Monazite is proven to be resistant to diffusion of U, Th, Pb and REE at temperatures lower than 800°C (Cherniak et al. 2004; Gardes et al. 2006). Consequentially this property leads to preservation of compositional domains, even through high-grade metamorphic events. Retentive domains thus represent age of formation and/or recrystallisation. Information gained by linking age to reaction can be placed into greater context when combined with existing knowledge about the P-T evolution path from other methods and mineral studies.

2.3 Zircon

Zircon is a silicate mineral with the chemical formula $ZrSiO_4$ that integrates trace amounts of U, Th, Hf, and REE into its crystal structure (Hoskin & Schaltegger 2003). The two U decay systems ($^{235}U{\rightarrow}^{207}Pb$ and $^{238}U{\rightarrow}^{206}Pb$) and their differing half-lives make it into a viable geochronometer. These two decay schemes can be used not only to date the time of crystallisation but can also be used to investigate Pb-loss (open system behaviour) and mixing of age domains during analysis (Bowring et al. 2006). The high closure temperature of the U-Pb system in zircon (>800°C) makes it useful for dating high-temperature geological events (Harley et al. 2007).

Zircon most commonly appears as an igneous mineral in igneous rocks where its occurrence is related to the Si-saturation of the rock; it is most common in rocks of higher Si-saturation (Hoskin & Schaltegger 2003). Metamorphic zircon occurs either as newly formed grains in high-T metamorphic environments or as partly recrystallised grains inherited from the protolith; the latter occurrence may appear in both high and low-grade metamorphic environments (Hoskin & Schaltegger 2003; Harley et al. 2007). Zircon crystals are durable with respect to many geological processes and may appear as detrital grains in sediments and sedimentary rocks, originating in such cases from weathered igneous and metamorphic rocks (Hoskin & Schaltegger 2003).

The differing processes behind formation of metamorphic zircon and monazite in high-T environments may allow refined geological interpretations based on the obtained geochronological dates (Harley et al. 2007). Keeping this in mind and utilising the combined strengths of two geochronometers may compensate for the weaknesses of both. For example, if both minerals are dated in a high-grade metamorphic rock, monazite and zircon may provide ages of peak metamorphism and post-metamorphic near-peak cooling respectively (Harley et al. 2007). In this case the two dates would produce a time constraint of said metamorphic event, thus effectively providing more information regarding the geological history than they would separately.

2.4 Geochronology

Isotopic dating

Geochronology makes use of radioactive decay systems and measurements of isotopic ratios in rock-forming and accessory minerals as well as whole-rock analyses to determine geological dates. Commonly used decay systems are Rb-Sr, K-Ar, $^{40}Ar/^{39}Ar$, K-Ca, Sm-Nd, and U-Th-Pb. These decay systems have different uses depending on half-lives, host mineral and P-T conditions of the rock and its geological history. These parameters decide what kind of event the resulting date is most likely to represent. Often, it can be relevant to use several geochronometers for one rock to compare dates of the different decay systems. Geochronological dates are used to make interpretations and set time constraints for geological events such as crystallisation of igneous minerals, mineral growth during metamorphism, or cooling.

When using an accessory mineral for geochronology it is assumed that the accessory phase has remained a closed system throughout its history. In short, if a mineral is exempt from further incorporation

of a parent isotope, intermediate daughters, and final stable isotopic product after crystallisation (and until present day) then it is referred to as a closed system (Faure & Mensing 2005; Schoene 2013). If loss or addition of any radioactive parent, intermediate daughter, or daughter isotopes takes place after crystallisation of the mineral, then it is referred to as an open system (Schoene 2013).

U-Th-Pb Decay

The U-Th-Pb geochronometer utilises the decay of three radioactive parent isotopes with differing half-lives; [235]U, [238]U, and [232]Th. These decay through a series of intermediate daughter isotopes to their respective stable radiogenic daughter isotopes [207]Pb, [206]Pb and [208]Pb (Schoene 2013). Due to the long half-life of U and Th this geochronometer can be used to acquire very old geological dates.

The half-lives of the parent isotopes are in this case much longer than that of the intermediate daughters; this enables a state known as secular equilibrium to be attained. Secular equilibrium means that stable daughter isotopes are produced at the same rate at which the parent isotope at the beginning of the chain decays (Schoene 2013). This in turn implies that the number of stable daughter isotopes in the sample is equal to the number of parent isotopes that have decayed (Faure & Mensing 2005). The number of stable daughter isotopes will continue to increase until they reach an equal amount of parent isotopes originally present as long as the system remains closed.

The following age determining equation makes use of the number of parent (N) and daughter (D) isotopes, the number of daughter isotopes incorporated during formation (D0) and the known decay constant of the radioactive parent isotope (λ) to calculate the time (t) since formation (Faure & Mensing 2005).

$$D = D_0 + N\left(e^{\lambda t} - 1\right) \quad [1]$$

This equation can be further developed to include isotopic ratios of elements in place of absolute values (N and D) where [204]Pb (nonradiogenic Pb) is used for normalisation.

$$\left(\frac{^{206}Pb}{^{204}Pb}\right) = \left(\frac{^{206}Pb}{^{204}Pb}\right)_0 + \left(\frac{^{238}U}{^{204}Pb}\right)\left(e^{\lambda 238t} - 1\right) \quad [2]$$

$$\left(\frac{^{207}Pb}{^{204}Pb}\right) = \left(\frac{^{207}Pb}{^{204}Pb}\right)_0 + \left(\frac{^{235}U}{^{204}Pb}\right)\left(e^{\lambda 235t} - 1\right) \quad [3]$$

$$\left(\frac{^{208}Pb}{^{204}Pb}\right) = \left(\frac{^{208}Pb}{^{204}Pb}\right)_0 + \left(\frac{^{232}Th}{^{204}Pb}\right)\left(e^{\lambda 232t} - 1\right) \quad [4]$$

Monazite incorporates a negligible amount of Pb during crystallisation allowing simplification of the aforementioned equations using only radiogenic lead (Schoene 2013).

$$\left(\frac{^{206}Pb}{^{238}U}\right) = \left(e^{\lambda 238t} - 1\right) \quad [5]$$

$$\left(\frac{^{207}Pb}{^{235}U}\right) = \left(e^{\lambda 235t} - 1\right) \quad [6]$$

$$\left(\frac{^{208}Pb}{^{232}Th}\right) = \left(e^{\lambda 232t} - 1\right) \quad [7]$$

These three equations each give an individual geological date. The two U equations can in turn be combined to form yet another equation used to calculate a geologic date using the ratio of [206]Pb and [207]Pb (Schoene 2013).

$$\left(\frac{\left(\frac{^{207}Pb}{^{204}Pb}\right) - \left(\frac{^{207}Pb}{^{204}Pb}\right)_0}{\left(\frac{^{206}Pb}{^{204}Pb}\right) - \left(\frac{^{206}Pb}{^{204}Pb}\right)_0}\right) = \left(\frac{^{235}U}{^{238}U}\right)\left(\frac{e^{\lambda 235t}}{e^{\lambda 238t}}\right) = \left(\frac{^{207}Pb}{^{206}Pb}\right) \quad [8]$$

Mineral zoning and mixing of age domains

Zoning occurs when a mineral grows and forms a layer or rim that is compositionally different from the pre-existing material. This can be a result of change in bulk rock composition or change of physical conditions, to favour a different chemical composition of the mineral in question. Zoning can be identified through different methods, for example BSE-imaging using SEM, where zones of differing chemical composition can be identified in greyscale. The zones in a mineral may record individual geological dates representing crystallisation (if formed at different times), known as age domains. Zoned minerals can cause complications during analysis if the zones are overgrown or if they are small and in close proximity to each other. A date will be meaningless if materials of different ages are mixed and analysed as one and the same.

3   Petrography

Samples used in the present study consist of fifteen thin sections (Table 1). These samples were used to date zircon by Piñán-Llamas et al. (2015). The hand samples are from three localities of quartzofeldspathic migmatite gneiss referred to as localities A (Fig. 3), B (Fig. 4), and C. The migmatite consists of two domains, leucosome and mesosome, which differ in mineralogy and texture. The leucosome formed through partial melting during metamorphism. It has a sugary texture and is composed primarily of quartz and K-feldspar giving it a red colour. The mesosome is the unmodified remnant of the rock and is distinguished by its rich sillimanite content giving it a grey colour. The primary objective was to locate and document monazite grains of two textural types described by Olsson (2013) found in the leucosome and mesosome respectively. Three of the fifteen potentially monazite bearing thin sections were selected for analysis (below).

Table 1. Study samples consisting of fifteen thin sections from Localities A, B, and C. Sil = Sillimanite. Grt = Garnet. Mnz = Monazite. Zr = Zircon.

Quartzofeldspathic migmatite gneiss				
Thin section	Locality	Leucosome / Mesosome	Minerals of interest	Comment
09-SGC-1	A	L + M	Sil, Grt, Mnz	
09-SGC-2a	A	L + M	Sil, Grt, Mnz	
09-SGC-2b	A	L + M	Sil, Grt, Mnz	
09-SGC-3	A	L + M	Sil, Grt, Mnz	
09-SGC-3a(1)	A	L + M	Sil, Mnz	
09-SGC-3a(2)	A	L + M	Sil, Mnz	
09-SGC-3b	A	L + M	Sil, Grt, Mnz	Focus for study
09-SGC-3c	A	L + M	Sil, Grt, Mnz	Focus for study
09-SGC-4	A	L	Mnz and/or Zr	Chloritised
09-SGC-20a	B	M	Sil, Mnz	
09-SGC-20b	B	M	Sil, Mnz	Focus for study
09-SGC-21	B	L	Mnz and/or Zr	Chloritised
09-SGC-10	C	L	Mnz and/or Zr	
09-SGC-11a	C	M	Mnz and/or Zr	
09-SGC-11b	C	M	Mnz and/or Zr	

Fig. 3. Photograph of Locality A showing K-feldspar-rich sillimanite-bearing quartzofeldspathic migmatite gneiss with parasitic folds (folded foliation marked S1) defined by sillimanite, biotite and opaques. Photograph by Leif Johansson. Reproduced from Piñán-Llamas et al., 2015, with permission from Elsevier.

3.1 Locality A: Sillimanite-bearing quartzofeldspathic migmatite gneiss

Most thin sections (excluding sample 09SGC-4) are dominated by quartz-feldspar leucosome with seriate-interlobate to granoblastic texture, interspersed with swaths, streaks and patches of sillimanite-rich mesosome. Needle-like sillimanite constitutes a parallel oriented foliation and/or lineation that has been subject to folding (marked S1 in Fig. 3). Sillimanite bundles occur together with biotite, garnet and opaque grains; locally sillimanite aggregates are radiating. Both leucosome and mesosome contain small amounts of biotite, opaque phases (ilmenite and hematite), and garnet. Retrograde muscovite laths are locally present in small amounts. Zircon and monazite are accessory phases. Due to the presence of both textural types of monazite (large zoned grains and small rounded; Olsson, 2013), samples 09-SGC-3b and -3c were chosen for further study.

09SGC-3b

The leucosome in sample 09SGC-3b is dominated by quartz and K-feldspar with granoblastic texture. Sillimanite-rich mesosome appears as foliae (Fig. 5). Biotite and opaque grains in the mesosome are larger (c. 2 -4 mm) and distinctly anhedral compared to their appearance in the leucosome (c. 20-200 μm). Inclusions with high relief and interference colours were observed within biotite grains. Monazite grains in the leucosome are small (c. 10-100 μm) and euhedral. Larger (c. 50-400 μm) monazite grains are found in sillimanite-rich mesosome; some of these grains are surrounded by an orange-stained corona of very fine-grained minerals (not identified).

09SGC-3c

As with sample 3b, leucosome is dominated by quartz and K-feldspar forming a seriate-interlobate to granoblastic texture. Small (c. 80-200 μm), subhedral to rounded garnet grains are found in the leucosome. Swaths of sillimanite-rich mesosome cover approximately half the thin section (Fig. 5). Anhedral biotite, garnet and opaque phases are present in the mesosome. Symplectite of quartz + biotite are present, appearing as rounded and elongated blotches. Inclusions with high relief and interference colours were observed within biotite grains, most likely monazite or zircon grains. Monazite grains in the mesosome are relatively large (c. 100-300 μm) and anhedral compared to the smaller (c. 10-100 μm) euhedral-subhedral grains in the leucosome. This sample has the highest amount of monazite of the investigated samples.

3.2 Locality B: Sillimanite-bearing quartzofeldspathic migmatite gneiss

This rock unit is dominated by mesosome; leucosome is sparse. Samples from this locality consist primarily of quartz and K-feldspar leucosome with streaks and patches of sillimanite-rich foliae. Biotite and opaque phases occur scattered throughout the samples; garnet is not present. Accessory phases are muscovite (retrograde), zircon and monazite.

09SGC-20b

The sample is free of sugary leucosome and consists of quartz and K-feldspar with streaks and patches of sillimanite-rich mesosome (Fig. 5). Small (c. 10-50 μm) grains of zircon and monazite occur scattered throughout the sample. Larger (c. 100-200 μm), complex monazite grains are present in sillimanite-rich foliae. Biotite grains and opaque phases have euhedral -subhedral texture.

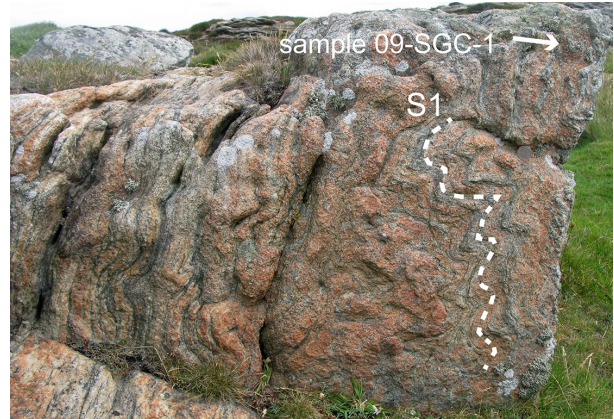*Fig. 4.* Photograph of Locality B showing sillimanite-bearing quartzofeldspathic migmatite gneiss with parasitic folds. The leucosome-poor sample from which thin sections 09-SGC-20a and b were produced lies just on top of the hammer head. Photographed by Leif Johansson. Reproduced from Piñán-Llamas et al., 2015, with permission from Elsevier.

3.3 Locality C: Quartzofeldspathic migmatite gneiss

Two thin sections were made from this rock unit, 09SGC-11a and -11b. These samples consist of relatively fine-grained (c. 0.5-1 mm) quartz and K-feldspar with a seriate-interlobate to granoblastic texture. There are biotite grains and opaque phases but no garnet. Muscovite (retrograde), zircon and monazite are accessory phases. A third sample, 09SGC-10, was taken from a discordant leucosome pod adjacent to this outcrop. This sample is coarser grained than sample 09SGC -11 (c. 2-4 mm) and features retrograde biotite with a greenish-chloritisised appearance.

4 Monazite texture

4.1 Methods

Energy-dispersive X-ray (EDX) analysis coupled to scanning electron microscopy was used for identification of minerals and their chemical composition, using a Hitachi S-3400N, fitted with an EDX analyser from Oxford Instruments and INCA software, at the Department of Geology, Lund University. With high magnification down to μm scale and a 1-2 μm spot size it is possible to analyse minor details such as zoning, rims, cores and lamellae of single mineral grains. Samples investigated by SEM must be electrically conductible and thus samples have to be prepared beforehand. In the case of thin sections these can be coated with a thin film of carbon or gold. An electron beam is focused and accelerated through a series of condenser and objective lenses from a source (electron gun; Hafner 2007). The electron beam strikes the sample producing signals consisting of secondary electrons, backscattered electrons, and X-rays (Hafner 2007). Detectors set up inside the sample chamber receive the signals, producing an image or compositional spectrum through accompanying software.

Produced images are known as Back Scattered Electron (BSE) images. These images are in greyscale, the brightness reflecting the atomic weight of elements. The difference in contrast depends on the amount of electrons reflected off the surface of the sample. Atoms with higher atomic number have higher charge thus reflect more electrons and appear brighter (Richter 2013).

The wavelengths of reflected X-rays are unique to each element (Richter 2013). Energy Dispersive X-Ray analysis (EDX) utilises reflected X-rays to produce a spectrum representing the chemical composition of the analysed sample.

During analysis, voltage was set to 15 kV and a Co-standard was used for calibration. Thin sections were carbon coated to a thickness of c. 2-3 nm to make them electrically conductive. Because of the high content of heavy elements in monazite, brightness and contrast could be set so that it was the only visible mineral in BSE.

4.2 Results

BSE-images of monazite grains from samples 09SGC-3b, -3c, and -20b reveal differences in both shape and internal texture. Monazite grains in the mesosome tend to have anhedral morphology with embayments and complex interior zoning (Fig. 6). Monazite grains in the leucosome are rounded with less complex internal zoning, either seemingly homogenous or with a core-rim structure (Fig. 6). The core of monazite grain 3bA1 in Figure 6 has concentric zoning that is truncated by a rim overgrowth and is the only discovered grain with this feature. The greyscale tone of cores and rims is not coherent, appearing bright in some grains and dark in others, and vice versa. The cores of leucosome grains are more distinct and euhedral than their mesosome counterparts. Internal zoning seemingly follows resorbed rims in parts of some grains (3cB3, top half dark zoning of 3cE2, and 3bM1 in Fig. 6) but appears truncated in others (left side of 3cE2 and lower right of 3bM1 in Fig. 6)

5 LA-ICP-MS

In situ U-Th-Pb was performed on selected grains in the thin sections described above, using LA-ICP-MS (Laser Ablation Inductively Coupled Plasma Mass Spectrometry; Schoene 2013).

5.1 Instrument and theoretical description

The four main constituents of the LA-ICP-MS instrument are laser, ablation cell, inductively coupled plasma and mass spectrometer (Fig. 7; Richter 2013). This analytical method has a number of advantages: it has the capability of measuring a wide array of elements, low detection limits down to ppt (parts-per-trillion), variable spot size (c. 5-750 μm depending on instrument), and analysis time of mere minutes. The laser is used to ablate the surface of the sample and
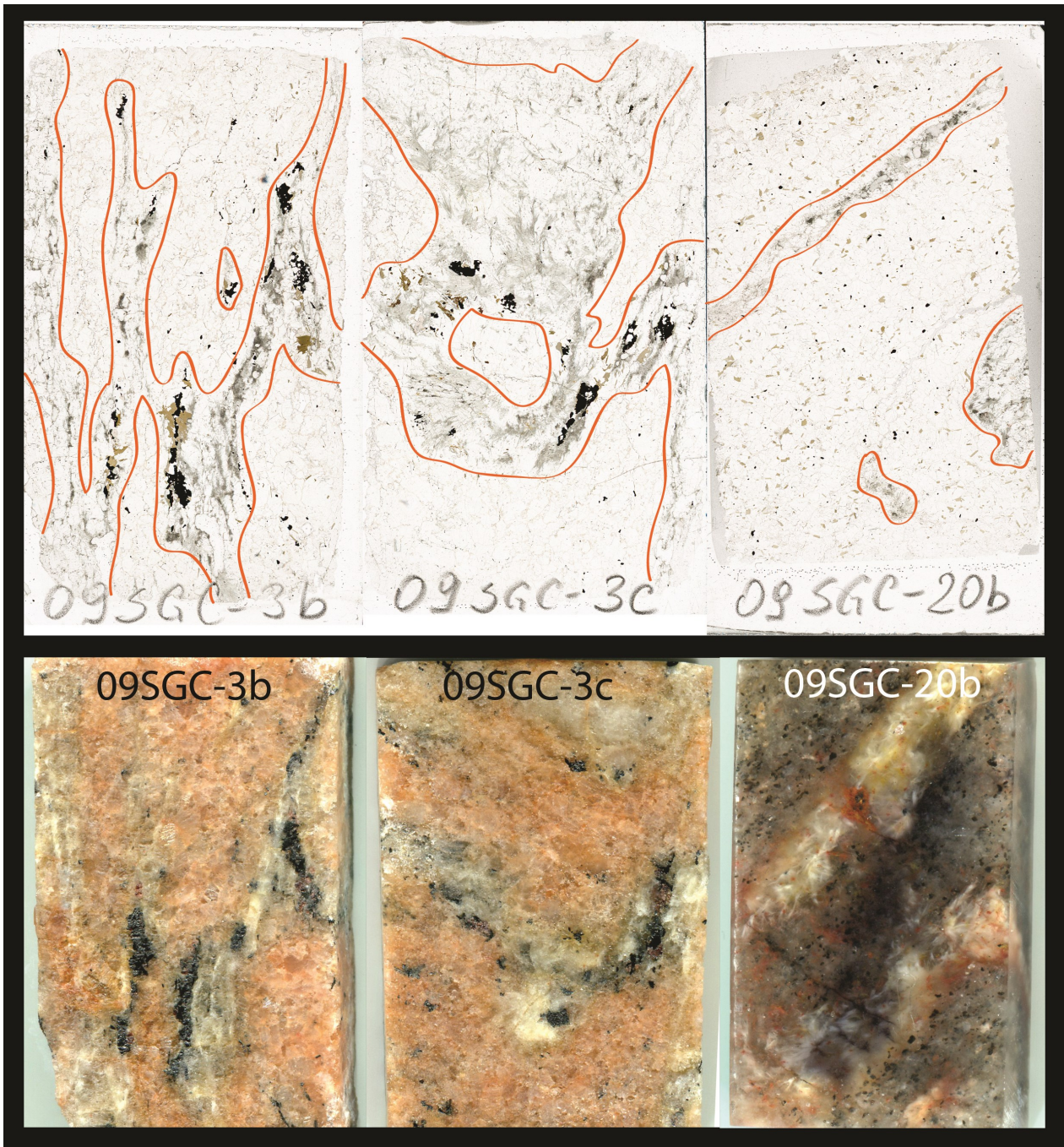
Fig. 5. Scanned images of thin sections 09SCG-3b (left), -3c (middle), and -20b (right) and rock chips from which they were made. Mesosome and leucosome are separated by red lines in thin section scans. Mesosome can be identified by sillimanite streaks (grey/white) as well as large biotite and opaque grains (brown/black). Leucosome consists primarily of quartz and K-feldspar (colourless in thin section, red in rock chips). The leucosome of samples 09SGC-3b and -3c are very difficult to tell apart from the mesosome of sample -20b in thin section, the most distinct difference being more biotite and opaques in sample -20b. The differences are more noticeable between the rock chips.
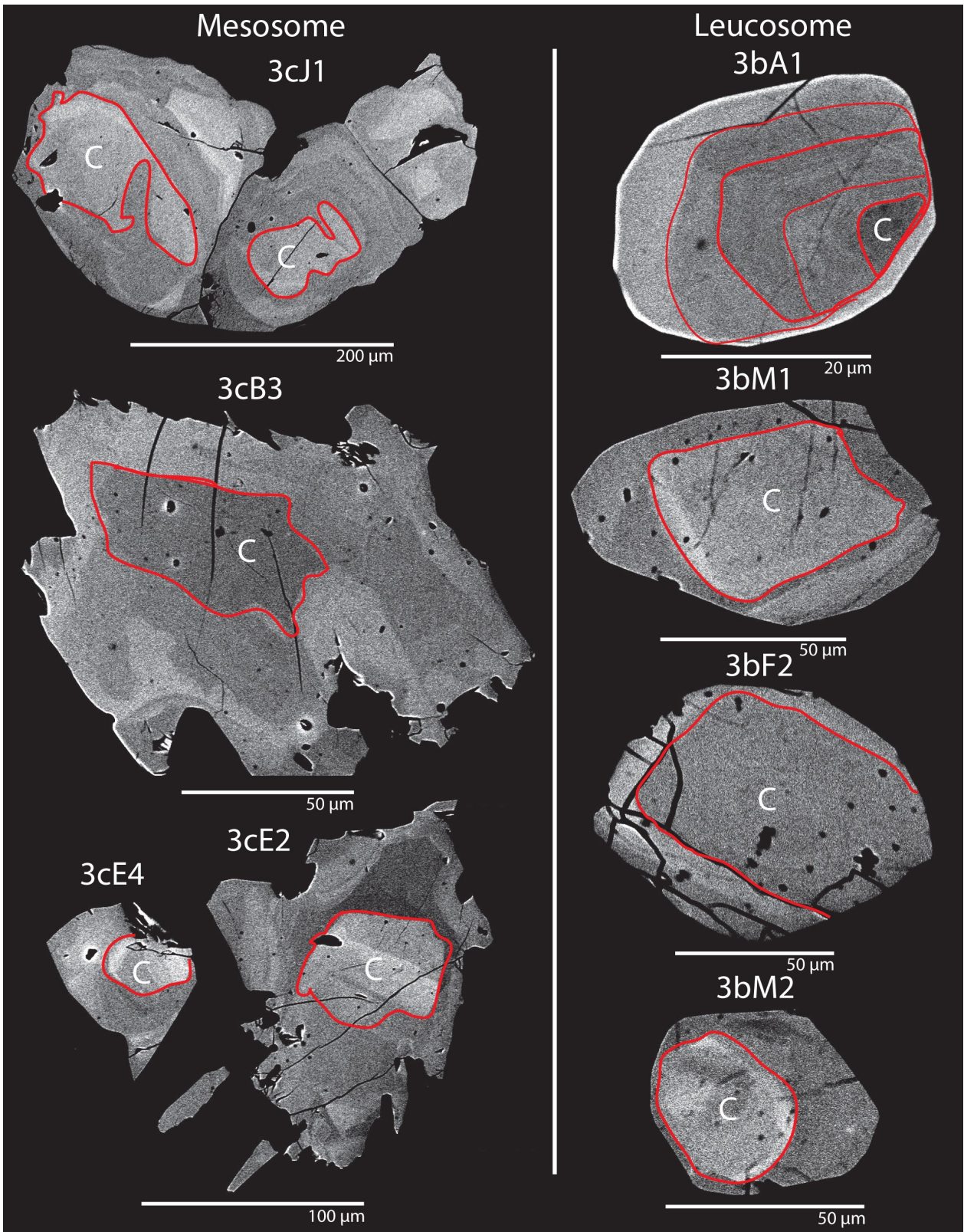
Fig. 6. BSE-images of monazite grains from mesosome (left) and leucosome (right). Overhead labels indicate the sample (09SGC-3b and -3c). Internal domains interpreted as distinct cores are outlined in red and marked "C".

produces an aerosol consisting of nanometre-scale particles. A carrier gas (e.g. Ar or He depending on the instrument) is flushed through the ablation cell picking up and transporting the aerosols into the ICP. A separate Ar gas flow forms plasma through electrical heating (induction) up to 10000°K, which then breaks down and ionises the aerosols (Primer 2005). Resulting ions enter the mass spectrometer (MS), which is held at a low pressure through a set of metal cones. Ions are accelerated and separated from photons and neutral material through electrostatic lenses (ion lens) before reaching the MS (Primer 2005). The MS consists of an ion lens, mass analyser and an ion counter (detector).

There are several types of mass analysers; one will briefly be mentioned here. The quadrupole, one of the most common mass analysers in ICP-MS, separates ions based on their mass to charge ratio by passing both direct and alternating current through four parallel rods set up to form a square (Longerich & Diegor 2001; Primer 2005). The mass analyser focuses ions of specific mass to charge ratios into the detector, which counts electrical pulses and produces a mass spectrum (Primer 2005). The precision and accuracy of LA-ICP-MS analysis can be compared with XRF (X-Ray Fluorescence) and EPMA (Electron Probe Micro-Analysis; Günther & Hattendorf 2005).

Parts of the LA-ICP-MS instrument introduce problems such as mass discrimination of isotopes (Horn et al. 2000) and elemental fractionation between Pb and U during analysis. Both of these error sources are counteracted by the application of what is known as external and internal corrections using a standard, a sample of which the age and isotopic ratios are known (Jackson et al. 1997; Ketchum et al. 2001; Kundsen et al. 2001; Kosler & Sylvester 2003).

5.2 Operation parameter

The ICP-MS used in this study is an Agilent 8800 (Kasapolu et al., 2016) located at the Department of Earth Sciences, Gothenburg University, Sweden. REE analysis used a spot size of 12 μm and laser specs of 10 Hz and 7.8 J/cm^2 to measure the relative abundance of ^{139}La, ^{140}Ce, ^{141}Pr, ^{146}Nd, ^{147}Sm, ^{153}Eu, ^{157}Gd, ^{159}Tb, ^{163}Dy, ^{165}Ho, ^{166}Er, ^{169}Tm, ^{172}Yb, and ^{175}Lu. Isotope measurements of U, ^{232}Th, ^{206}Pb, ^{207}Pb, ^{208}Pb, ^{175}Lu and ^{89}Y used a spot size of 10 μm with the laser running at 5 Hz and 5.77 J/cm^2. Because monazite incorporates only negligible amounts of ^{204}Pb, this isotope was not measured during analysis. The chosen spot size created some difficulty in analysing smaller grains and complex domains but was for the most part sufficient. In some cases very small monazite grains were completely vaporised by the laser before the full analysis was completed. A final setup of 5 μm spot size and laser specs of 5 Hz and 5.77 J/cm^2 was run to more precisely analyse small domains and grains.

Analyses were interspersed with two shots of each standard. The gap between standard and sample analyses was extended as time passed from every six

to every twenty measurements before measuring standards again.

Isotope and trace element amounts were measured in CPS (counts per second) as the LA-ICP-MS instrument is configured to measure isotope ratios and not absolute concentrations. CPS data were converted to concentration (ppm) using the software Iolite (Iolite 2011; conducted by Tomas Naeraa, Department of Geology, Lund University). Converted elements are ^{89}Y, ^{175}Lu, ^{206}Pb, ^{207}Pb, ^{208}Pb, and ^{232}Th. ^{238}U/^{235}U is considered to be at a constant value of 137.88 to 1 in terrestrial material, which means that there is very little ^{235}U compared to ^{238}U. For that reason the abbreviation U is used to represent an approximate total concentration of both isotopes.

5.3 Preparation and procedure

The main purposes of LA-ICP-MS analysis of monazite grains in rocks from Stensjöstrand were to obtain U-Th-Pb dates and document possible variations in chemical composition between different generations of monazite. Analysis was made directly in thin section, in order to relate composition to textural position of individual grains. Three thin sections were prepared for this task: 09SGC -3b, -3c, and -20b.

During LA-ICP-MS analysis the field of view was restricted to a 1 mm wide window, viewable only in reflective light. Therefore, locations of different monazite grains were determined beforehand using microscopy and SEM. Polarised microscopy was used in order to locate the largest monazite grains, but smaller grains were impossible to tell apart from zircon. Complementary mineral confirmation was achieved through spot EDX analysis. This data was not used for other means than mineral identification. Grains equal to or larger than 10μm in size were documented (a size constraint is set by the spot size of the LA-ICP-MS). BSE-images were taken of individual grains together with the surrounding texture. These images also revealed zoning patterns and were taken in high magnification. Reflected light images were taken for reference. The monazite grains were marked on A3 printed scans of the thin sections and images were compiled in Microsoft PowerPoint for easy access and observation during LA-ICP-MS analysis.

Half a day of preparation and one day of LA-ICP-MS analysis were spent at the Department of Earth Sciences in Gothenburg, May 2015. Sample preparation involved removal of carbon coating and cleaning the surface of thin sections, mounting the sample holder (Fig. 8), and recording the locations of monazite grains using computer software. Having locations stored beforehand allowed for efficient analysis thereafter. Grains in different samples, of varying sizes and complexity with differing textural locality were analysed to cover the full range of monazite types in both leucosome and mesosome.
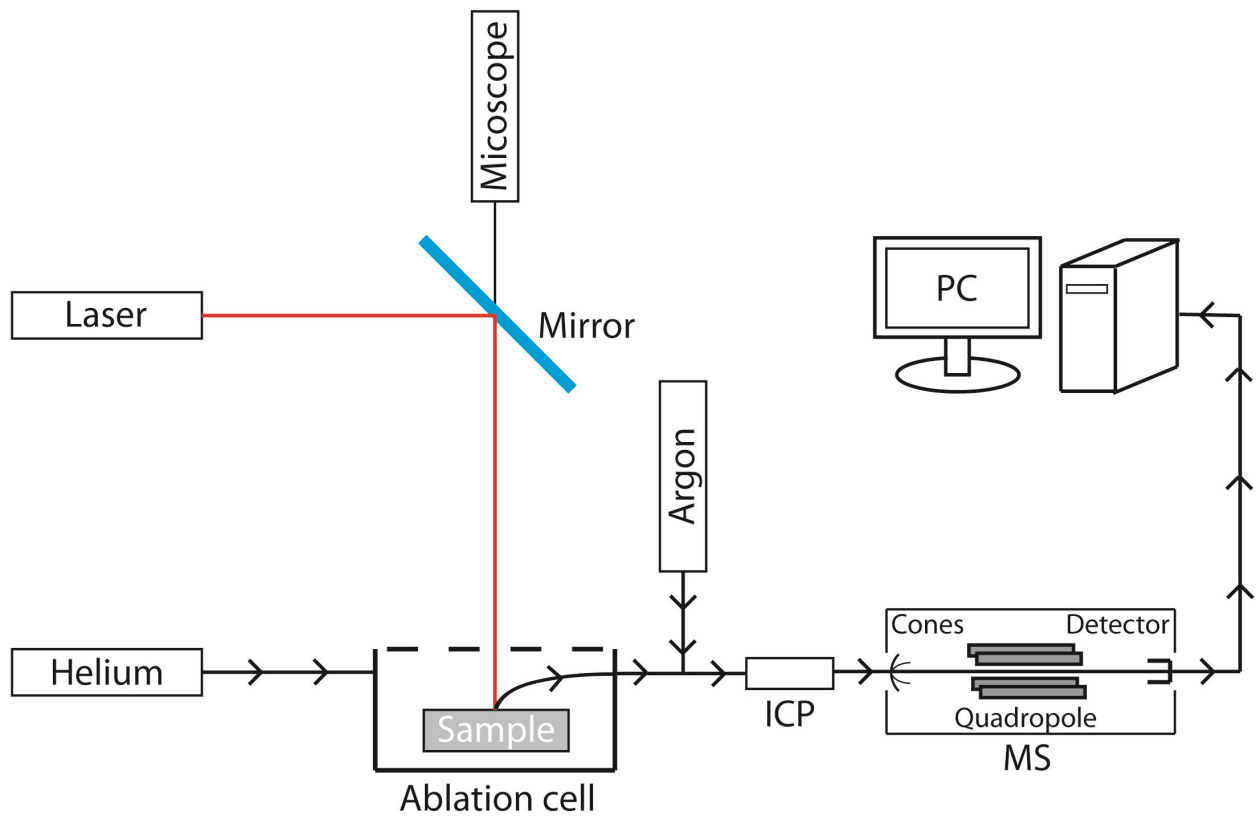
Fig. 7. Sketch of the principal components of an LA-ICP-MS instrument (Modified after diagram from Richter, 2013).
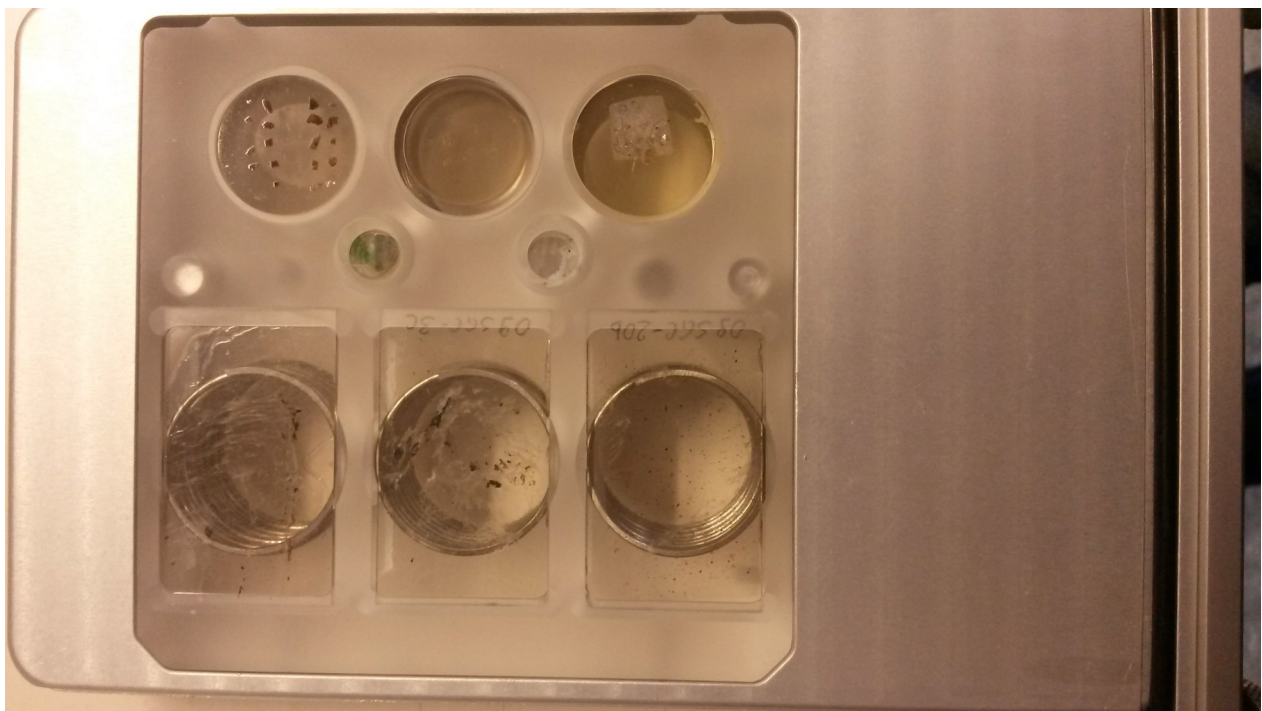

Fig. 8. Cell sample holder for LA-ICP-MS at the Department of Earth Sciences, Gothenburg. Top three circular mounts contain standards. Bottom three rectangular slots hold thin sections: (from left to right) 09SGC-3b, -3c, and -20b.

5.4 Data reduction

Raw data was reported 2σ standard deviation and processed by Tomas Naeraa at the Department of Geology, Lund University, using Iolite (Iolite 2011). Data was reduced by investigation of the signal during each measurement and manual selection of the most stable plateau. Monazite 44069 was set as the primary reference standard for data reduction with Moacir and TMM as secondary standards (further details in section 5.6.). Reduced data was then processed and organised in Microsoft Excel with the aid of Isoplot add-in (Ludwig 2012).

REE data processing was done by Thomas Zack, Department of Earth Sciences, University of Gothenburg, using the software Glitter (Glitter 2005). NIST SRM glass sample 610 (National Institute of Standards and Technology; Standard Reference Materials; Kane 1998), monazite standard Moacir (Gasquet et al. 2010), and monazite and xenotime standards Djupedal (Jakobsson 2014) were utilised for correction of element fractionation of REE analyses as well as for converting CPS to ppm using Glitter software (Appendix Fig. 1; Glitter 2005).

5.5 Visualisation of data

Geochronological U-Th-Pb dates can be visualised for easier processing in a number of ways. Wetherill and Tera-Wasserburg concordia diagrams are the most common diagrams as they can be used for age calculation as well as for tests of Pb-loss and mixing.

Wetherill Concordia

The Wetherill concordia (also known as conventional concordia), named after its creator, can be used to display the effects of open systems (Wetherill 1963; Wetherill 1973). The isotopic ratios $^{206}Pb/^{238}U$ and $^{207}Pb/^{235}U$ are plotted against each other producing a so-called concordia curve consisting of points representing solutions to equations 5 and 6 in section 2.4 Geochronology, *U-Th-Pb decay* (Faure & Mensing 2005; Schoene 2013). The curve is a result of the different half-lives of ^{235}U and ^{238}U, the prior being shorter, leading to higher $^{207}Pb/^{235}U$ ratios over time (Richter 2013; Schoene 2013). Dates that plot on this curve are said to be concordant and have as such remained closed systems since formation, meaning that $^{206}Pb/^{238}U$ and $^{207}Pb/^{235}U$ ratios have developed along the curve.

Tera-Wasserburg Concordia

An approach different from the conventional concordia diagram is the Tera-Wasserburg concordia diagram (also known as inverse concordia diagram) originally developed during a study of lunar rocks with excess ^{206}Pb, ^{207}Pb and ^{208}Pb (Tera & Wasserburg 1972). This concordia plots $^{238}U/^{206}Pb$ and $^{207}Pb/^{206}Pb$ on the x- and y-axis respectively to produce a concordia curve. Data is interpreted similarly to conventional concordia plots.

Concordance

Concordance is a relative measure of correlation between two different isotopic dates. It can be calculated by dividing the two different isotopic dates (e.g. $^{206}Pb/^{238}U$ and $^{207}Pb/^{206}Pb$) and multiplying the result by 100, i.e. $(^{206}Pb/^{238}U)/(^{207}Pb/^{206}Pb)*100$. It is used to argue for the validity of isotopic dates based on the fact that, if data plots concordantly, both isotopic dates should be exactly the same and will thus plot on the concordia curve.

The difference in concordance between conventional and inverse concordia plots is assumed to not have large implications, as Kenneth R. Ludwig (2012) writes in the user manual for Isoplot: "Tera-Wasserburg concordia diagrams are mathematically equivalent to conventional concordia diagrams. Tera-Wasserburg plots can have advantages in visualisation, however, because the errors in their X- and Y-values are generally much-less correlated than those of the conventional concordia diagram, so that the relative scatter of their error ellipses is more (visually) apparent." In short: the most concordant points on the conventional concordia plot are the most concordant points on an inverse concordia plot.

Discordance

Dates will be discordant if the sample in question has met the criteria for an open system at some point in time during its existence. Discordance means that the Pb/U ratios plot off the concordia curve. This can be caused by loss or gain of Pb and U as well as age mixing (Schoene 2013). A case of Pb loss in a suite of minerals and its development over time is presented in Figure 9a. Pb leaving the system is in this case assumed to maintain the same $^{207}Pb/^{206}Pb$ composition as the mineral had at this point in time (i.e. Pb did not fractionate). Minerals that lost ALL radiogenic Pb in recent time plot at origin as their geochronological clocks were reset. Those that suffered varying degrees of Pb loss in recent time plot on a line between the concordant dates of the rock and origin. As time moves on, the latter linear relationship of discordance is maintained because new radiogenic Pb is created at the same rate throughout all the mineral phases. One billion years later the minerals that plotted in origin at the time of Pb loss now yield a date of that event. Those grains that did not lose radiogenic Pb (plotted concordantly) still yield a date of crystallisation. Discordia can extend above the concordia curve for some minerals (monazite for example) as a result of U loss (Faure & Mensing 2005).

Figure 9b illustrates the same case as Figure 9a using an inverse concordia plot. Figure 9c illustrates a case where the dated minerals are contaminated with ^{204}Pb. In such a case, the intercept would plot much higher and provide an inaccurate date (Ludwig 1998). Recent Pb loss or U/Pb calibration error causes horizontal displacement of data points on an inverse concordia (Fig. 9d). Briefly explained, Pb loss would result in a horizontal shift as a response to a decreased

$^{238}U/^{206}Pb$ ratio (horizontal shifting to the right; left if U gain). The $^{207}Pb/^{206}Pb$ would remain unchanged provided that the lost Pb did not fractionate, preventing vertical shift.

MSWD

MSWD is short for mean square weighted deviation which is, according to Ludwig (2012): "…roughly, a measure of the ratio of the observed scatter of the points (from the best-fit line) to the expected scatter (from assigned errors and error correlations)"; in short, an assessment of how well the calculations fit the data. An MSWD value close or equal to 1 (also referred to as unity) implies that there is a high correlation between scatter and error of the data points. Higher MSWD values can be interpreted as an underestimation of analytical error while lower values can be interpreted as an overestimation of analytical errors. The MSWD value is mainly is used to quantify if analysed samples are from one age population or represent a mix of two or several populations.

5.6 Standards

Three monazite standards were used for this study: 44069 (Aleinikoff et al. 2006), Moacir (Gasquet et al. 2010), and TMM (Thompson Mine Monazite; Williams et al. 1996; Buick et al. 2010). Standard data and their source material were obtained from Richter (2013; Table 2).

Table 2. Data for standards 44069, Moacir, and TMM. Table modified after Richter, 2013.

Standard	Age ± 1σ [Ma]	Method	Reference
44069	424.9±0.04	TIMS	Aleinikoff et al. (2006)
	426.0±3.0	SHRIMP	
Moacir	504.3±0.2	TIMS	Gasquet et al. (2010)
TMM	1766.0±0.3	TIMS	Wiliams et al. (1996)
	1766.0±13.0	LA-ICP-MS	Buick et al. (2010)
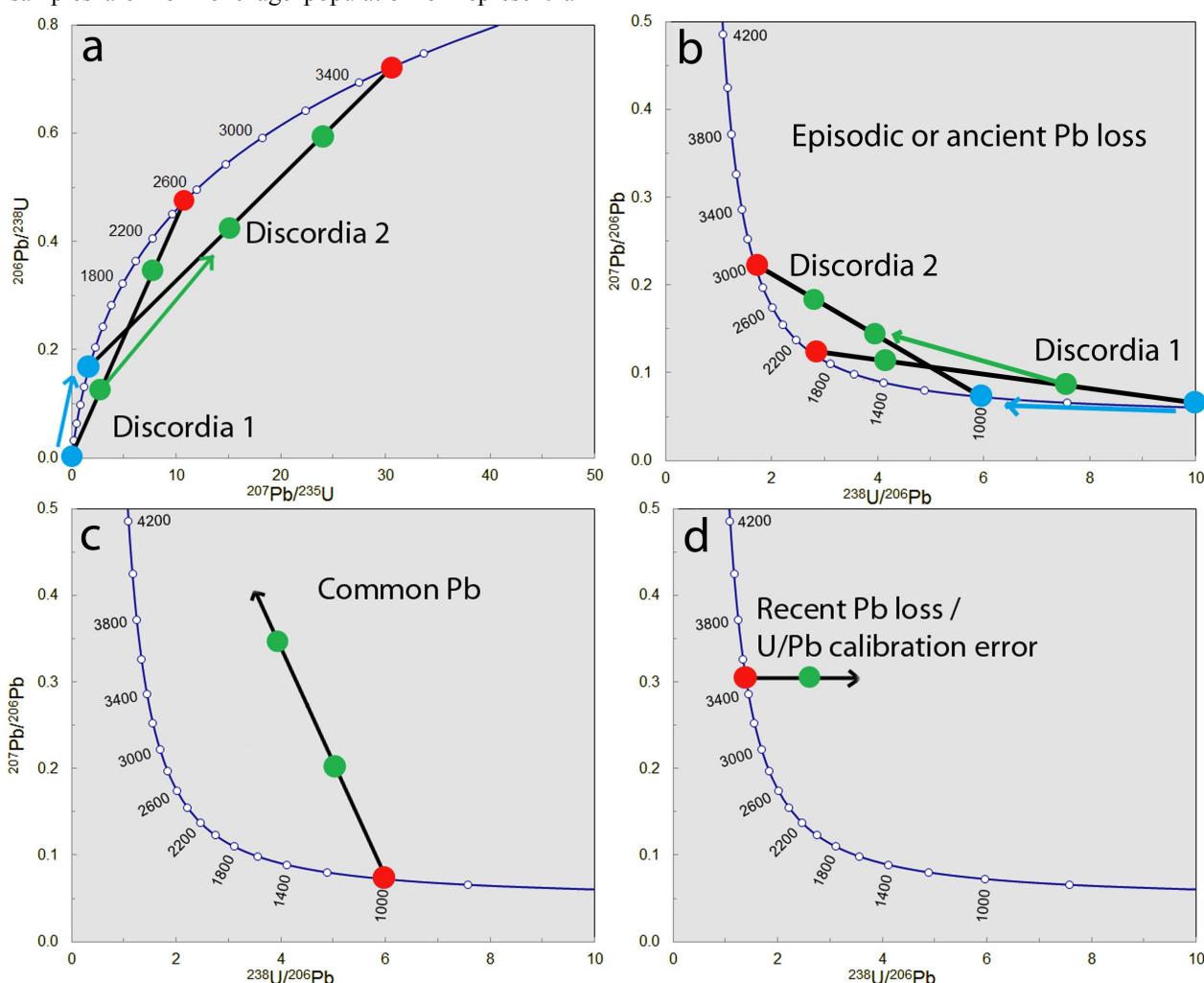
Fig. 9. Conventional and inverse concordia diagrams illustrating discordia due to Pb loss. Numbers along the concordia curves represent million years in the past. Red dots represent minerals that produce concordant dates and did not suffer Pb loss. Blue dots represent minerals that lost all radiogenic Pb at some point in time. Green dots represent minerals that suffered varying degrees of Pb loss. a & b) Two illustrations of the same Pb loss case using conventional and inverse concordia plots respectively. c) Illustration representing a case of discordia caused by ^{204}Pb contamination. d) Illustration representing a case of recent Pb loss or U/Pb calibration error using inverse concordia plot. Plots were produced in Isoplot add-in for Excel (Ludwig 2012) and modified in Adobe Photoshop.

44069

Monazite 44069 originates from a meta-sedimentary rock unit, with psammitic to pelitic gneiss and schist constituents, located in the Wilmington Complex, Delaware (USA; Aleinikoff et al. 2006). The source rock was metamorphosed in the amphibolite-facies at 424.9 ± 0.04 Ma (TIMS), which is the age of the monazite (Table 2; Aleinikoff et al. 2006). The 44069 monazite grains on the mount used in this study are chemically homogenous, show no zoning, and are c. 100 μm in size (Aleinikoff et al. 2006; Richter 2013).

Moacir

Moacir originates from the Itambé pegmatite district located on the São Fransisco craton, Brazil (Seydoux-Guillaume et al. 2004). These samples are chemically homogenous, without fluid or solid inclusions, and consist of c. 200-400 μm fragments (Seydoux-Guillaume et al. 2002; Richter 2013). The age of Moacir relates to the Pan-African orogeny, which took place c. 650-450 Ma, and two pegmatite-forming events, one syntectonic at c. 560 Ma and one post-tectonic at c. 500 Ma (Table 2; Viana et al. 2003; Richter 2013).

TMM

TMM is of Canadian origin, specifically from The Thompson Nickel Belt of Manitoba, and is part of the Archean Superior craton (Richter 2013). This region is characterised by poly-metamorphosed orthogneisses and migmatites (Rayner et al. 2006; Richter 2013). The first event involved plutonism and metamorphism in a continental arc environment at c. 1880 Ma (Percival et al. 2004, 2005; Rayner et al. 2006), the second crustal thickening and plutonic intrusion associated with craton collision and resulting in peak metamorphism at c. 1840-1780 Ma (White et al. 2002; Zwanzig & White 2002; Machado et al. 2011). The third and final phase involved pegmatite intrusions at c. 1765 Ma (Rayner et al. 2006; Table 2)

5.6.1   Results of anlyses of reference material/ standards

Age determination

Nineteen analyses of the primary standard 44069 resulted in concordant data; one discordant point was rejected for both intercept and weighted average date calculations. The weighted average $^{207}Pb/^{206}Pb$ date of 411 ± 8.8 Ma and upper intercept date of 426 ± 7.3 differ by c. 15 Ma although both have acceptable MSWD values (Fig. 10a). The upper intercept date is close to the TIMS and SHRIMP dates achieved by Aleinikoff et al. (2006; 424.9 ± 0.4 Ma and 424.0 ± 3.0 Ma respectively).

Analyses of standards Moacir and TMM are more discordant than those of standard 44069. Analysis of Moacir yielded a weighted average $^{207}Pb/^{206}Pb$ date of 598 ± 29 Ma (Fig. 10b), which is considerably

higher than the 504.3 ± 0.2 Ma TIMS date by Gasquet et al. (2010). Analysis of TMM yielded a weighted average $^{207}Pb/^{206}Pb$ date of 1781 ± 9 Ma and an upper intercept date of 1794 ± 9 Ma (Fig. 10c), which are to be compared with 1766 ± 13 Ma LA-ICP-MS and 1766.0 ± 3.0 Ma TIMS dates measured by Buick et al. (2010) and Williams et al. (1996) respectively.

The relatively good correlation between for standard 44069 (Aleinikoff et al. 2006) means that the applied corrections for data reduction should be satisfactory.

Pb-loss trend

Analyses of all three standards show a linear drift reminiscent of a Pb-loss trend, the main difference being extension above the concordia. This trend is visible in both conventional and inverse concordia plots. According to Faure and Mensing (2005) an extension above concordia can be a result of U loss or erroneous U/Pb calibration during data reduction. The discordias are likely a result of downhole fractionation (Paton et al. 2010), a phenomenon resulting in continuously larger differences in U/Pb ratio as the laser ablates deeper through the sample because of the differences in atomic weight and distance to the mass spectrometer. This can also be seen in the weighted average plot of standard TMM where the $^{206}Pb/^{207}Pb$ isotopic dates increase throughout the day of analysis (Fig. 10c).

5.7   Results

5.7.1   U-Th-Pb data

Age groups

The analytical data of samples 09SGC-3b, -3c and -20b reveal two age groups at 0.9-1.2 Ga and 1.3-1.5 Ga (Fig. 11). Data is plotted as 2σ error ellipses (also known as circle of uncertainty), either concordantly along the concordia curve or discordantly outside of the curve.

Monazite in mesosome and leucosome

The data shows the existence of grains consisting of two age generations, as well as grains of only a single generation (Figs. 12 and 13). Both types occur in the mesosome and the leucosome. Monazite grains that were analysed but did not produce concordant dates are shown in Appendix Fig. 2. Analysed monazite grains from sample 09SGC-20b are shown in Appendix Fig. 3.

Data selection and age calculation

Data points with a maximum normal discordance of c. 2% and maximum reverse discordance of c. 1.5% (based on $(^{207}Pb/^{235}U)/(^{206}Pb/^{238}U)$ concordance) were used for calculating weighted average dates. The $(^{207}Pb/^{206}Pb)/(^{206}Pb/^{238}U)$ discordance for the same points was larger, having a maximum normal discordance of c. 6.5% and a reverse discordance of up to c.

20
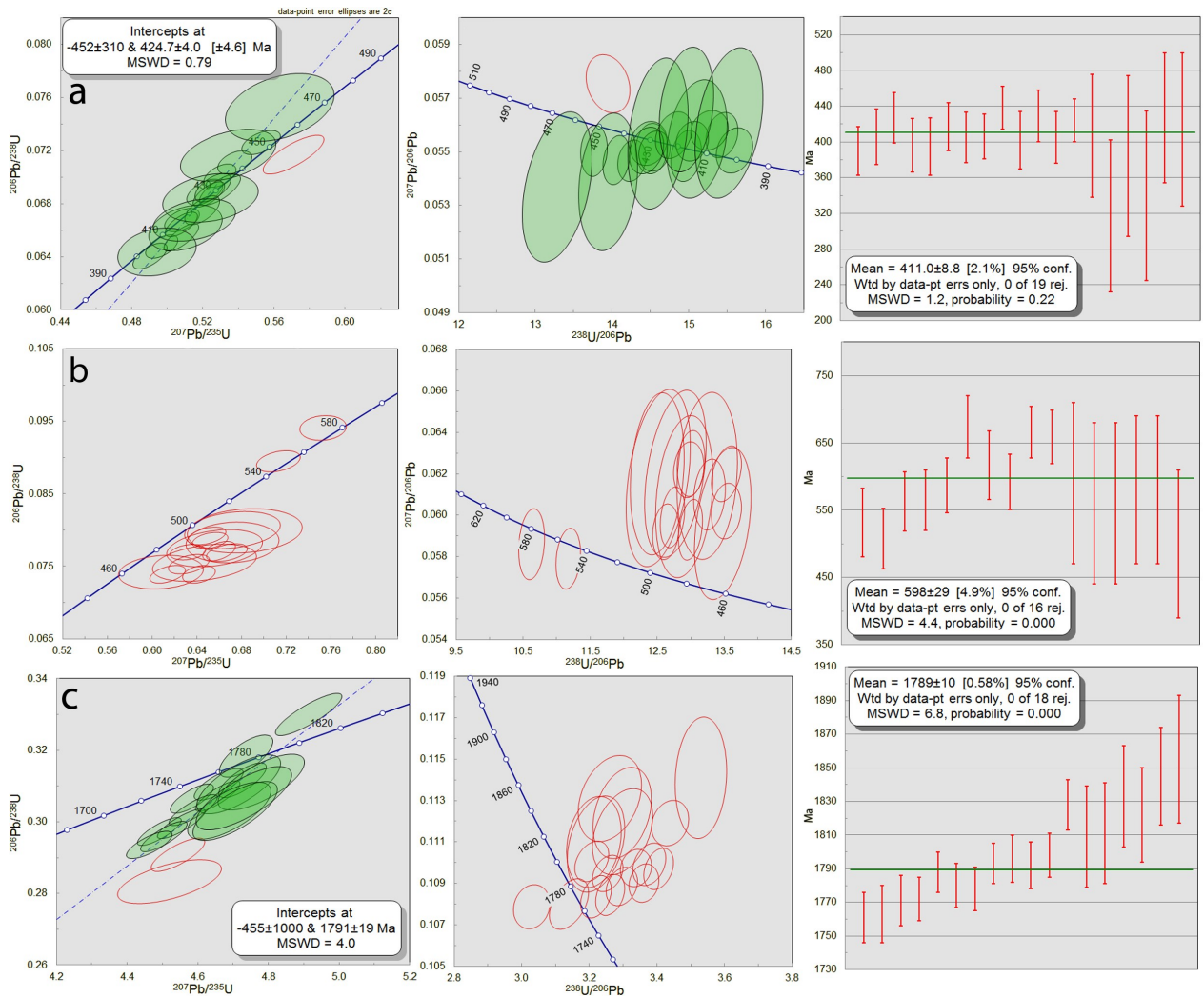
Fig. 10. Concordia and weighted average plots for standards 44069, Moacir, and TMM presented in rows a, b, and c respectively. Green transparent ellipses represent concordant points used in the intercept date calculations for standards 44069 and TMM, (a) and (c) respectively. The red ellipses represent discordant points rejected for intercept date calculation. The leftmost column shows conventional concordia plots. The centre column shows inverse concordia plots displaying the same data points as in the leftmost column. The rightmost column shows weighted average age calculation using $^{207}Pb/^{206}Pb$ isotopic dates.
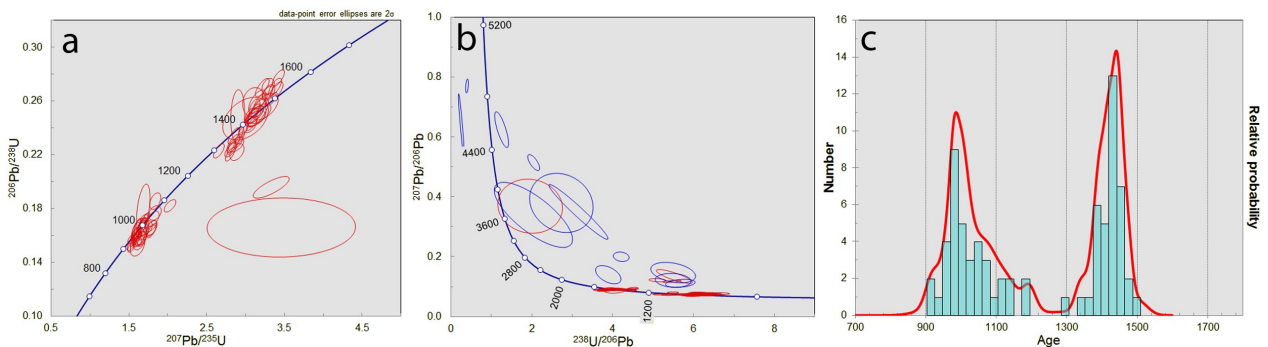
Fig. 11. a) Conventional concordia plotting all points excepting point 115 and those of sample 09SGC-20b. b) Inverse concordia plotting the data points displayed in (a), plus point 115 and extremely discordant dates acquired from sample 09SGC-20b (blue). c) Histogram density plot of $^{207}Pb/^{206}Pb$ dates, showing two distinct peaks at c. 983 Ma and c. 1442 Ma.

21
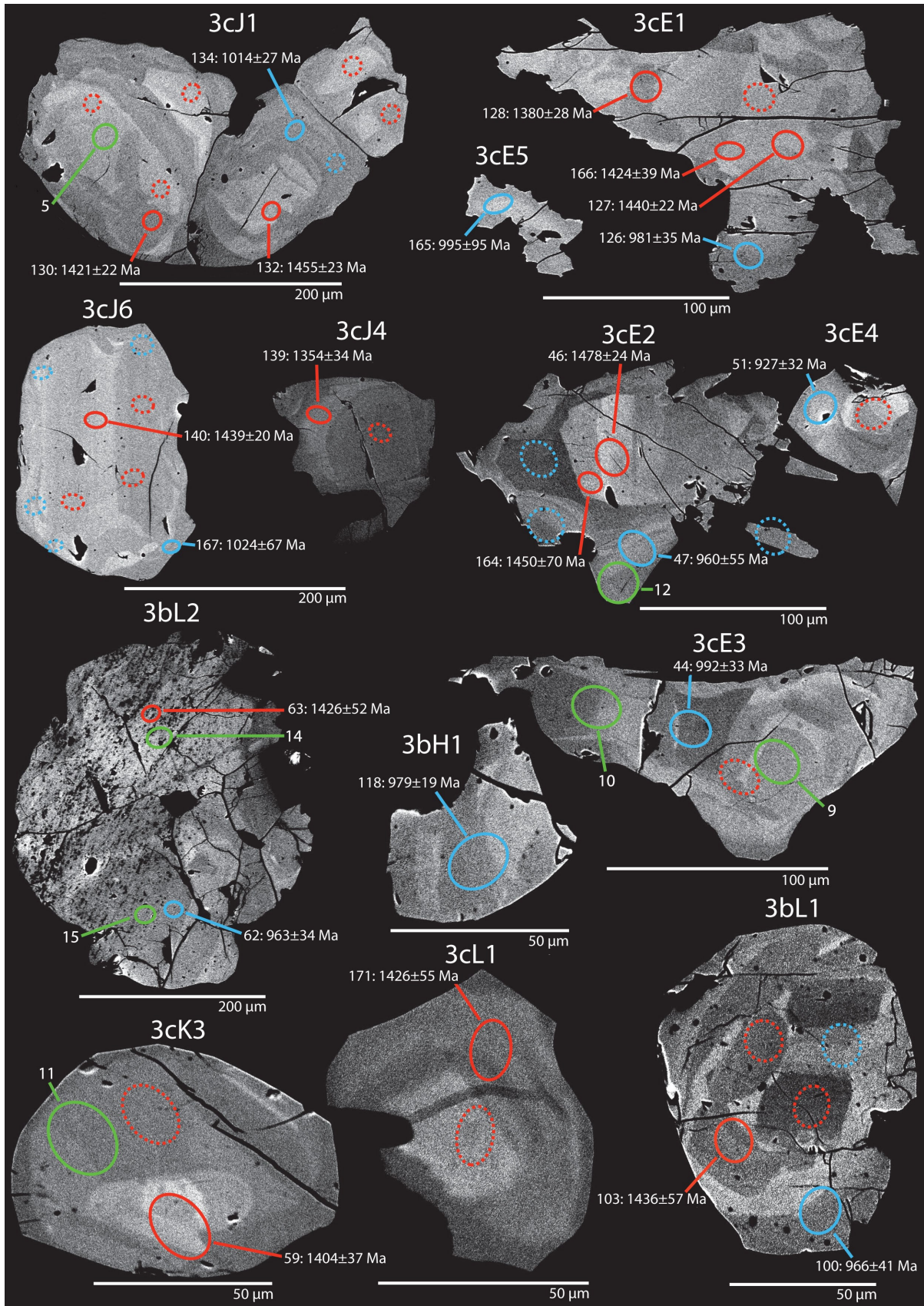
Fig. 12. BSE-images of analysed monazite grains in mesosome, with outlines of laser ablation pits, which were retrospectively traced over microscopy photographs. Overhead labels indicate the sample (09SGC-3b and -3c). Blue and red ellipses represent the 1.43 Ga and 0.99 Ga generations respectively. Concordant data points are reported with ^{207}Pb/^{206}Pb isotopic dates. Dashed ellipses represent discordant data points. Spot size is either 5 or 10 µm. Green ellipses represent REE analysis with a spot size of 12 µm and are marked with spot numbers.

22
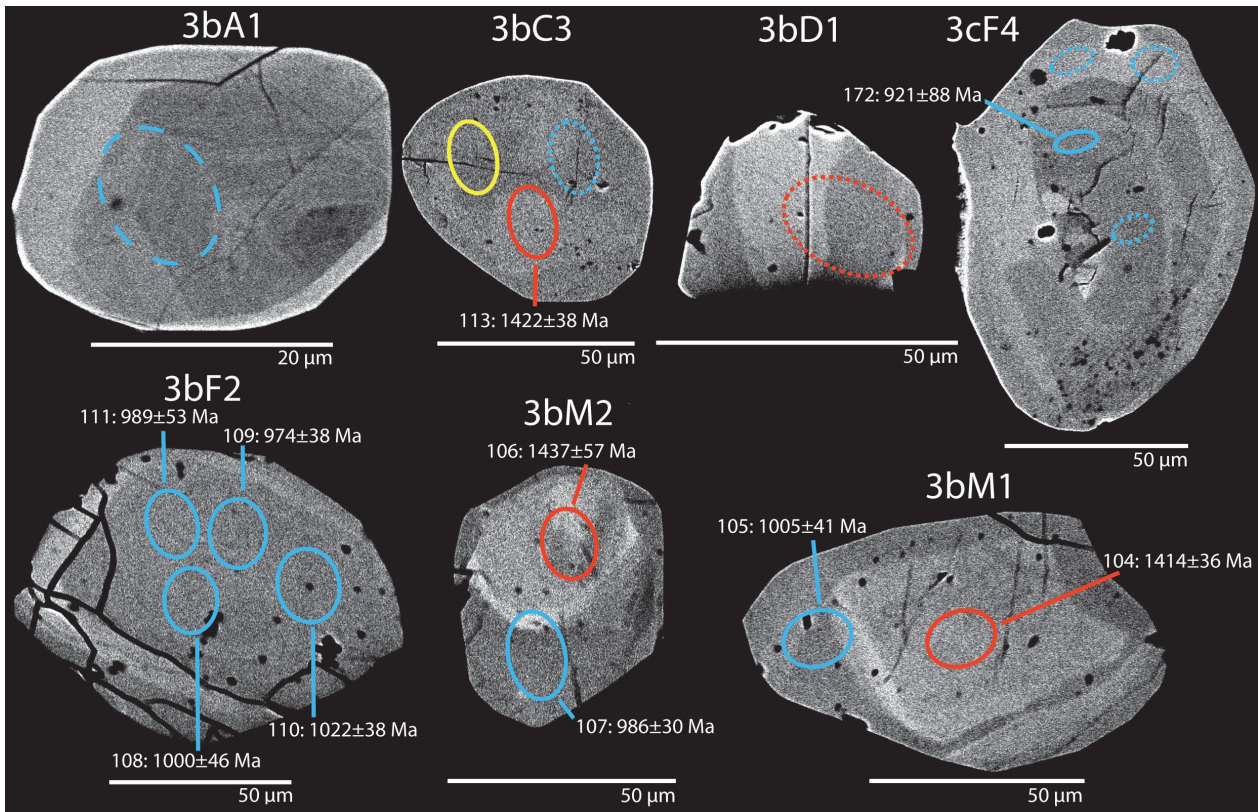
Fig. 13. BSE-images of all analysed monazite grains in leucosome with outlines of laser ablation pits, which were retrospectively traced over microscopy photographs. Overhead labels indicate the sample (09SGC-3b and -3c). Red and blue ellipses represent the 1.43 Ga and 0.99 Ga generations respectively. Concordant data points are reported with ^{207}Pb/^{206}Pb isotopic dates. The yellow ellipse represents a rejected data point. Spot size is either 5 or 10 µm.

7.5%. 18 out of 38 and 16 out of 37 points were chosen for the lower and higher bracket respectively.

Analyses with 5 µm spot size produced data with noticeably higher uncertainties than those of 10 µm due to lower count rates. This is illustrated in the concordia plots with larger error ellipses.

Four points were rejected during data reduction due to bad signals caused by partial or complete grain vaporisation before analysis was complete (87, 89, 112 and 115; Appendix Table 1). Measured isotopic ratios are presented in Appendix Table 2.

Analyses of monazite grains in sample 09SGC-20b had extremely high isotopic dates and errors as a result of very low U values. Only one analysis, out of thirteen, from this sample was within acceptable errors (Point 76 in Appendix Table 1; Appendix Fig. 3).

Weighted average using concordant isotopic dates was chosen, because the data was not concordant enough to calculate a concordia date. For a concordia date to be calculated it must be assumed that data points are equivalent (Ludwig 2012). This would be illustrated on a concordia plot by overlapping error ellipses. The spread of ellipses also resulted in difficulty to calculate an intercept date.

Four dates were calculated in total: both ^{206}Pb/^{238}U and ^{207}Pb/^{206}Pb dates for the two age groups respectively (Fig. 14). Results were ^{206}Pb/^{238}U dates of 1422 ± 22 Ma (MSWD=10.7) and 988 ± 17 Ma (MSWD = 10.5) and ^{207}Pb/^{206}Pb dates of 1434 ± 14 Ma (MSWD = 2.8) and 988 ± 11 Ma (MSWD = 1.2).

5.7.2 Trace elements including rare earth elements

Trace element analyses show trends of relative U enrichment and depletion of Y, Lu and Th in the 0.99 Ga monazite generation compared to the 1.43 Ga generation. The 0.99 Ga generation has a larger spread in U and lower range of Y and Lu contents (Fig. 15).

The chondrite normalised REE pattern in Figure 16 shows higher LREE relative to HREE, typical of monazite (Williams et al. 2007), as well as a negative EU anomaly. Data is presented in Appendix Table 3.

6 Discussion

6.1 Petrography

In the investigated monazite grains, zoning that is lighter in greyscale tone tends to have higher values of Th, Y, and Lu and lower values of U while the opposite tends to be true for darker tones. However, this correlation is not coherent between all grains.

The complex zoning and anhedral morphology of monazite grains in the mesosome indicates that they have been subject to recrystallisation and resorption processes during metamorphism (cf. Spear & Pyle
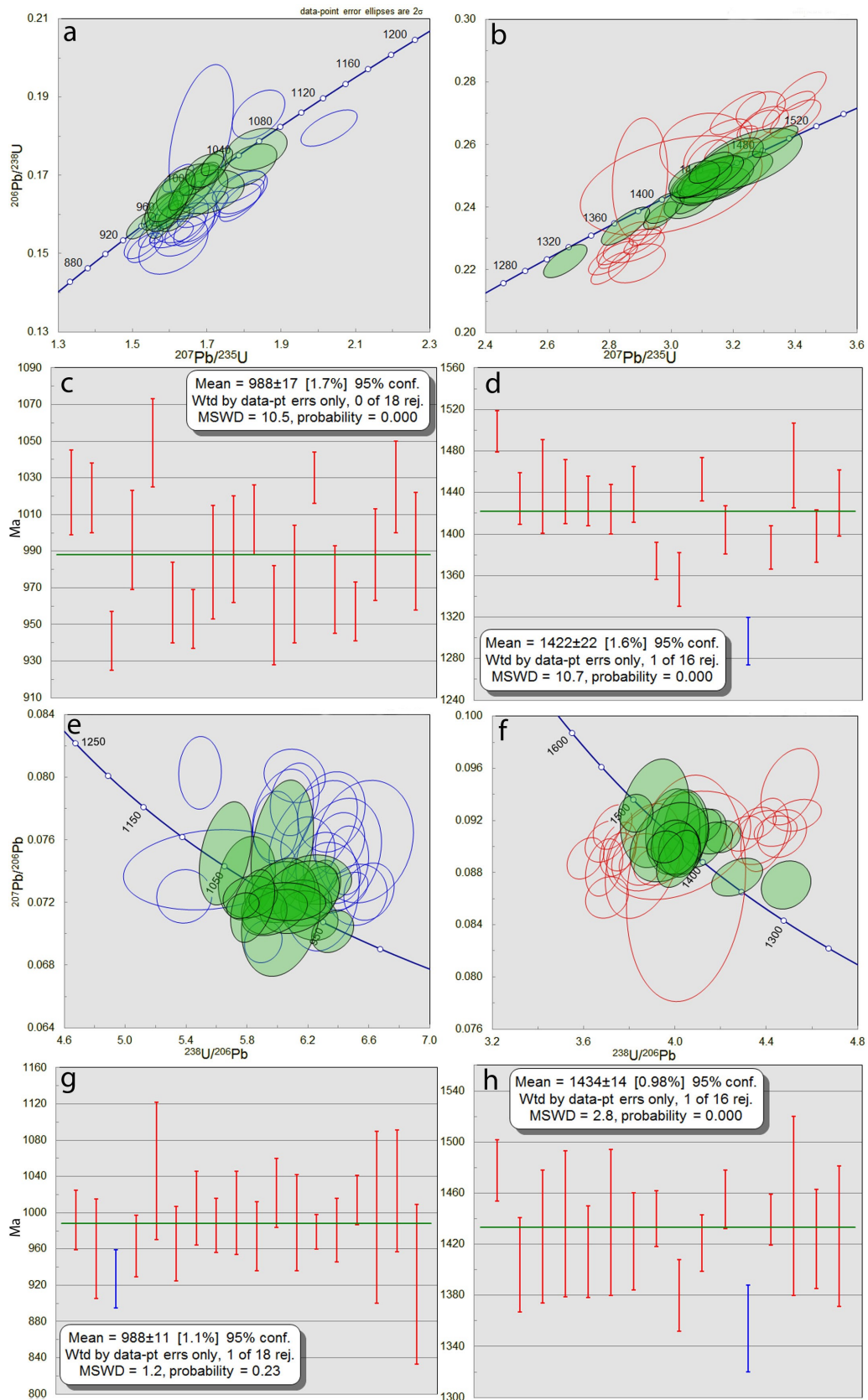
Fig. 14 . Concordia plots and age calculations based on reduced LA-ICP-MS data. Blue and red ellipses represent the two different age groups. Green transparent ellipses represent the most concordant data points that were used to calculate weighted average ages. Shown are calculated results with errors and number of points used/rejected. a & b) Conventional concordia plots of the two different age groups. c & d) Weighted average calculations using $^{206}Pb/^{238}U$ dates. Blue bar marks analysis rejected by Isoplot. e & f) Inverse concordia plots of the same data used for the conventional concordia plots (a & b). g & h) Weighted average calculations using $^{207}Pb/^{206}Pb$ dates.

2002); these processes, along with new mineral growth, may also be the cause for the ovoid shape and small size of the monazite grains in the leucosome (cf. Fraser et al. 2004). Resorption processes may lead to truncation of internal zoning, embayment textures in rims, or rounding of the mineral grain (Müller et al. 2010). The internal complexity of monazite grains in the mesosome may be the result of overgrowth, i.e. newly forming or recrystallising material filling in embayments and other textural irregularities of retentive and partially resorbed grains of the older generation monazite grains.

   The cores of monazite grains 3bD1, 3cF4, 3bM1, and 3bM2 in the leucosome are visually distinct in BSE-images (Fig. 13). Together with age results this suggests that these cores represent retentive and partially resorbed grains of the older generation (excepting monazite grain 3cF4, which only produced younger dates). The presence of older monazite in leucosome indicates that the mineral remained at least partially intact even in the Sveconorwegian melt phase, reflecting that monazite is a refractory phase (cf. Spear & Pyle 2002). Monazite grains composed exclusively of young generation material may have grown as new crystals during the Sveconorwegian orogeny rather than being merely recrystallised, while recrystallisation was possibly responsible for monazite grains composed of old generation cores and young generation rims.

6.2   U-Th-Pb data

The two age groups are evidence of two generations of monazite in the sillimanite-bearing quartzofeldspathic rocks at Stensjöstrand, dated at 1434 ± 14 Ma and 988 ± 11 Ma (Figs. 11 and 14). The age data of monazite

from Stensjöstrand can be compared with previously published zircon data from the same samples (Fig. 17; Piñán-Llamas et al. 2015). The zircon data was obtained by secondary ion mass spectrometry (SIMS), a method that yields higher precision than LA-ICP-MS analysis.

6.2.2   Hallandian age

The weighted average date of 1434 ± 14 Ma for monazite from Stensjöstrand corresponds with 1.43 Ga Hallandian ages achieved of metamorphic zircon in the Eastern Segment (Christoffel et al. 1999; Söderlund et al. 2002; Möller et al. 2007; Brander et al. 2012). Distinctly younger Hallandian ages were obtained by Piñán-Llamas et al. (2015) for zircon at Stensjöstrand: 1386 ± 7 Ma (Fig. 17) in the same sillimanite-bearing quartzofeldspathic migmatite gneiss sample (Locality A, thin sections 09SGC-3a-c) as investigated in this study, and nearby migmatitic garnet amphibolite (Hansen et al. 2015).

   The Hallandian age of zircon in the two different rocks at Stensjöstrand is c. 50 Ma younger than that of the monazites in this study. This suggests that conditions for monazite growth were met at an earlier stage in the P-T-t loop of the Hallandian orogeny than conditions required for zircon growth. Perhaps this was due to breakdown of phases such as allanite or garnet during change to higher P-T conditions that led to monazite-in reaction, although there is no petrographic evidence to directly support this theory. Another cause of the difference in age could be the apparent data drift in the results of this study, which may have produced older dates than what is actually representative of the rock. Cases of differing ages between monazite and zircon in the same rock have been noted in
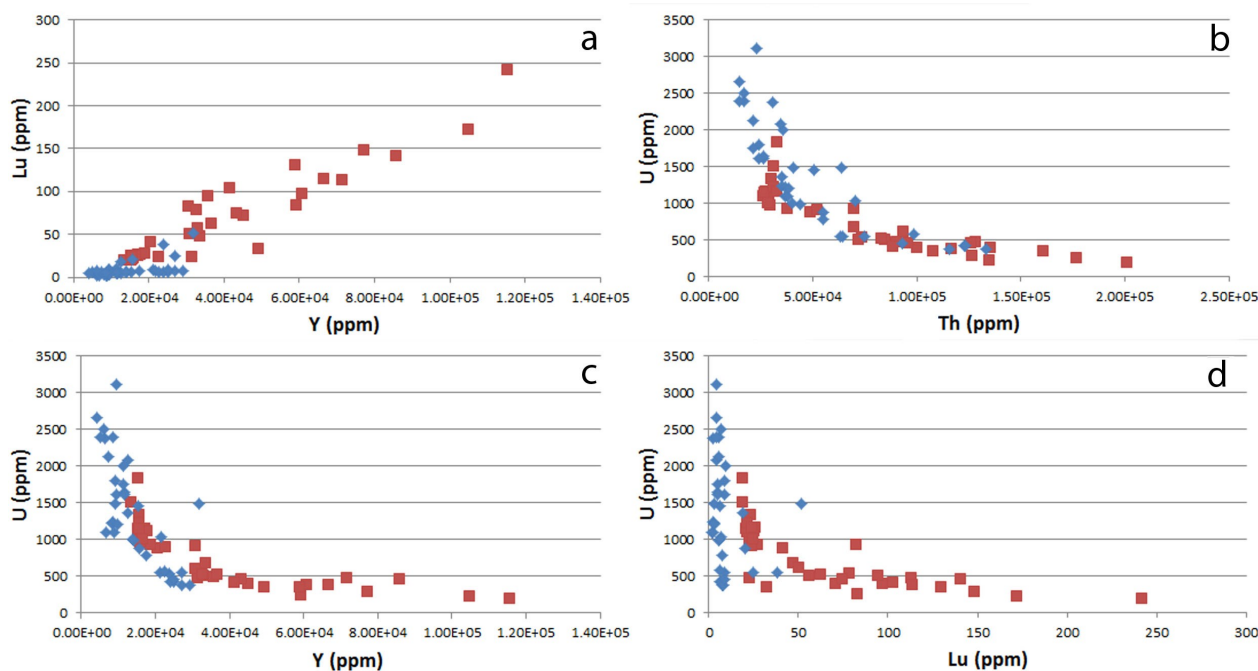
Fig. 15 . Scatter plots illustrating differences in element contents between the monazite generations. Red = 1.43 Ga generation. Blue = 0.99 Ga generation.
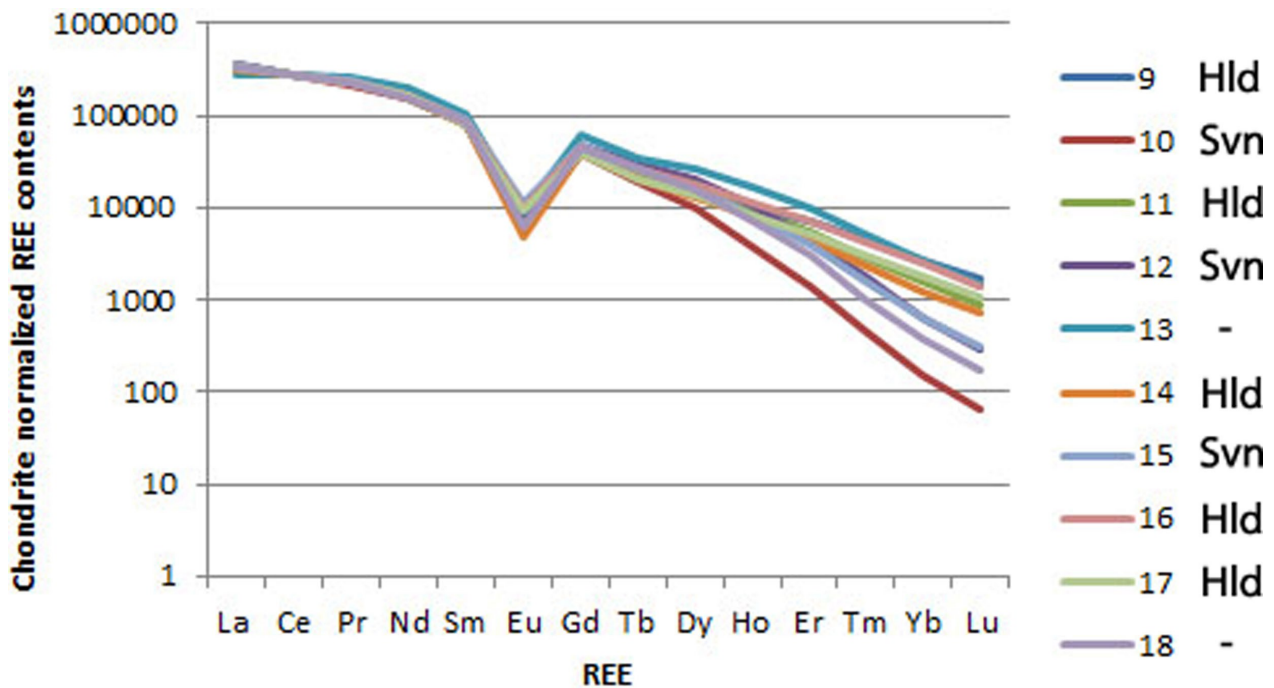
Fig. 16 . Masuda-Coryell diagram (Masuda 1962; Coryell et al. 1963) showing chondrite normalised REE contents in monazite from Stensjöstrand. Analyses 12 and 15 overlap, the former being barely visible. Hld = Hallandian generation. Svn = Sveconorwegian generation. Points of unknown generation are marked with a dash (-).

earlier studies (e.g., Rubatto et al. 2001; Zeh et al. 2003; McFarlane et al. 2006; Kelsey et al. 2008; Högdahl et al. 2012). These differences have been attributed to LREE supersaturation in melt-bearing rocks being controlled by complex processes other than dissolution of pre-existing monazite, which was indicated by monazite precipitating before, together with, or even after zircon in melt-bearing rocks (Högdahl et al. 2012).

6.2.3 Sveconorwegian age

The younger age of 988 ± 11 Ma for monazite from Stensjöstrand is c. 18 Ma older than the 970 ± 5 Ma age of the youngest zircon generation in the rocks, reported by Piñán-Llamas et al. (2015). This date coincides with two geological events in the Eastern Segment: Sveconorwegian high P-T metamorphism at 0.99-0.98 Ga (Johansson et al. 2001; Möller et al. 2015) and partial melting at 0.98-0.96 Ga (Andersson et al. 1999, 2002; Söderlund et al. 2002; Möller et al 2007, 2015; Hansen et al. 2015).

6.2.4 Protolith age

Protolith ages of c. 1.7 Ga (Piñán-Llamas et al. 2015) were not achieved from this study of monazite. 1.7 Ga monazite is however indicated by one analysis that hit a monazite inclusion in zircon in sample 09SGC-20b (data in Piñán-Llamas et al., 2015).

6.2.1 Domain mixing

Domain mixing during analysis has been of concern due to the internal complexity of certain monazite grains. The relatively small spot sizes (5, 10 and 12

μm) enabled good spatial precision in most of the larger grains. When examined retrospectively, laser pits are slightly larger than the beam size and could have led to unintentional ablation of adjacent domains during analysis. Moreover, domains may change at depth. If the topmost, visible domain is shallow or thin then the laser may ablate through and collect material from a separate domain, inclusion or mineral below it. Domain mixing may be responsible for producing the spread in dates seen in the data (Figs. 11 and 14; Appendix Table 1).

6.2.5 Data drift and Pb-loss trend

The data drift observed in the results of the standard analyses can also be seen in the results for the 1.43 Ga monazite generation (Figs. 10 and 14).

Calculating an intercept date through the linear drift of the 1.43 Ga monazite generation produces a date close to the $^{207}Pb/^{206}Pb$ weighted average date, with the downside of a worse best-of fit (MSWD; Fig. 18a). This calculation should be considered warily as it was produced for rough comparison with weighted average date and was as such subject to non-rigorous data reduction. The main point is that the intercept date falls within error of the weighted average date.

Figure 18c shows an inverse concordia plot of all data points with very large discordance, including all points from sample 09SGC-20b as well as 89, 112 and 115 from samples -3b and -3c. The main points of interest in this plot are the linear trends and lower intercepts. The lower intercepts roughly coincide with weighted average dates for the two respective generations of monazite (1.43 and 0.99 Ga). This relation could indicate that the monazite grains were subject to

26
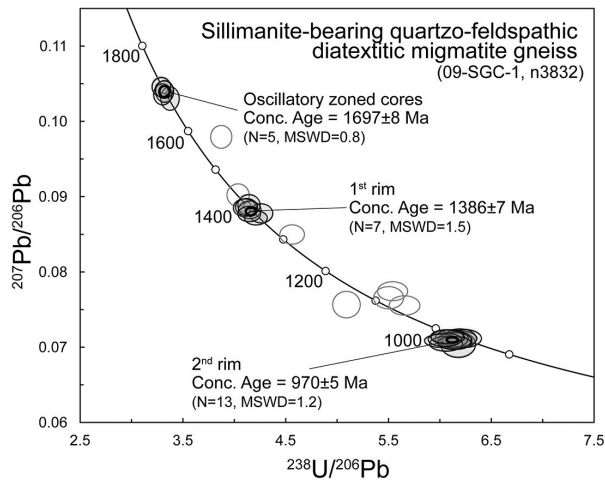
Fig. 17. Zircon geochronology (Piñán-Llamas et al. 2015) of the same sample (thin sections 09SGC-3a and -3c) as investigated in this study. Inverse concordia diagram of silli-manite-bearing quartzofeldspathic migmatite gneiss showing three zircon generations (diagram by Jenny Andersson). Reproduced with permission from Elsevier.

Pb or U-loss at some point in time or extreme down-hole fractionation during analysis. The low U values of monazite from sample 20b might hint toward U-loss (Appendix Table 1). The higher intercept date for this sort of trend should generally indicate at which point in time the Pb or U-loss event occurred but the extremely old dates of c. 4 Ga are not plausible for the rocks in this study, so Pb-loss is not feasible. However, a more plausible cause of the discordance could be ^{204}Pb contamination and an increased sensitivity to this due to extremely low amounts of U resulting in extremely high upper intercepts (Figs. 9c and 18c), although, since this isotope was not measured during analysis it is not possible to make a supported correlation. This data should in any case, due to extreme discordancy and large error ellipses, be subject to scepticism.

6.3 Trace elements including rare earth elements

Trace element data shows various trends when plotted against one another (Fig. 15). Hallandian monazite contains higher amounts of Y, Lu, and Th, while Sveconorwegian monazite is higher in U. The reason behind higher Y, Lu, and Th concentrations in the Hallandian grains may be that because they formed first, the matrix was depleted in these elements before growth of the second, Sveconorwegian, monazite generation. Another explanation would be formation of another mineral phase, e.g. garnet, with a stronger or similar affinity for these elements contending monazite for the trace element budget. Small amounts of garnet (<5%) are present in samples 09SGC-3b and -3c (none in -20b).

The overlap of trace element contents between old and young generations may indicate material exchange during a metamorphic event where recrystallisation of Hallandian monazite grains took place, i.e. breakdown of existing monazite to produce new monazite. Breakdown of garnet to provide material for monazite growth is another possibility. High U values in the Sveconorwegian generation could theoretically be caused by redistribution of U from U-oxides in fractures and grain boundaries, or through diffusion of disseminated occurrences in the mineral assemblage as a result of fluid migration during metamorphism (Heier 1979; Hassan et al. 1988). Breakdown or recrystallisation of zircon or allanite may, however, be more plausible sources of U, although petrologic evidence is not preserved in the samples.

The chondrite normalised REE plot shows higher LREE than HREE (Fig. 16). The difference in relative amounts can be explained by monazites high and low compatibility for LREE (higher) and HREE (lower) respectively. Points 10, 12, 15 and 18 plot somewhat lower in the HREE than the remaining points. Three of these can (arguably) be correlated with younger domains (except point 18; Fig. 16; Appendix Table 4). The differences in LREE between individual grains are actually larger than they seem when comparing to HREE. Neither of the monazite generations

Fig. 18. a) Conventional concordia with intercept date through points forming a Pb or U loss trend (green ellipses) of the old (1.43 Ga) generation of monazite. Red ellipses were not included in intercept calculation. b) Inverse concordia showing the same points as (a) forming a horizontal, linear trend. c) Inverse concordia with intercept dates showing all data points from sample 20b, points 112 and 115 from sample 3b and point 89 from sample 3c. Red and blue ellipses represent Hallandian (1.43 Ga) and Sveconorwegian (0.99 Ga) generations respectively.

shows depletion trends regarding LREE content as only point 13 shows values deviating from the norm and is also the only REE analysis from sample 20b (Fig. 19; Appendix Fig. 3); point 13 shows higher HREE than remaining analyses. Perhaps the higher amounts of REE in monazite 20bC1 are related to the lack of garnet in sample 20b.

Although, if this trend is indeed of any significance then it could indicate that the younger generation of monazite grew simultaneous with or after a HREE compatible phase, e.g. garnet, or simply that most of the HREE budget of the rock had been locked into the older generation of monazite.

The negative Eu anomaly (Fig. 16) is likely related to fractionation of Eu by feldspar. Trivalent REE are incompatible in plagioclase and potassium feldspar as opposed to divalent Eu (Rollinson 1993). Feldspar hosting the majority of the Eu budget in the rock would result with a negative anomaly in the monazite.

7   Conclusions

- Hallandian and Sveconorwegian metamorphic monazite are present in migmatitic sillimanite-bearing quartzofeldspathic gneiss at Stensjöstrand. It is impossible to distinguish between retentive and younger rims through BSE greyscale, and age analysis must be utilised.
- The two monazite generations correlate broadly with dates obtained from zircon (Piñán-Llamas et al. 2015) in the same sillimanite-bearing quartzofeldspathic migmatite gneiss, except for the c. 1.7 Ga generation of protolith or source zircon.

- Monazite and zircon geochronology yield slightly different dates. Monazite yielded 988 ± 11 Ma and 1434 ± 14 Ma. Zircon dates of 970 ± 5 Ma and 1386 ± 7 Ma were obtained by Piñán-Llamas et al. 2015.
- Resorption textures of monazite grains in the mesosome and trace element transitions between Hallandian and Sveconorwegian monazite indicate recrystallisation of Hallandian monazite.
- Hallandian monazite growth exhausted the REE budget resulting in less material for Sveconorwegian monazite.

8   Outlook
Suggestions to follow-up this study:
- Compositional analysis of orange-stained corona and fine-grained mineral aggregates to learn more about the low-grade retrograde history.
- Follow-up study of remaining samples from Localities B and C. Why was the U content of sample 09SGC-20b monazite grains extremely low? Do Hallandian and Sveconorwegian generations of monazite appear in other rocks at Stensjöstrand? Does protolith generation monazite appear in the Eastern Segment?
- Correlation of chemical composition to BSE zoning can be improved by line scans or element X-ray mapping of entire monazite grains. This can also be done with garnet to more closely investigate relationship between the two minerals.
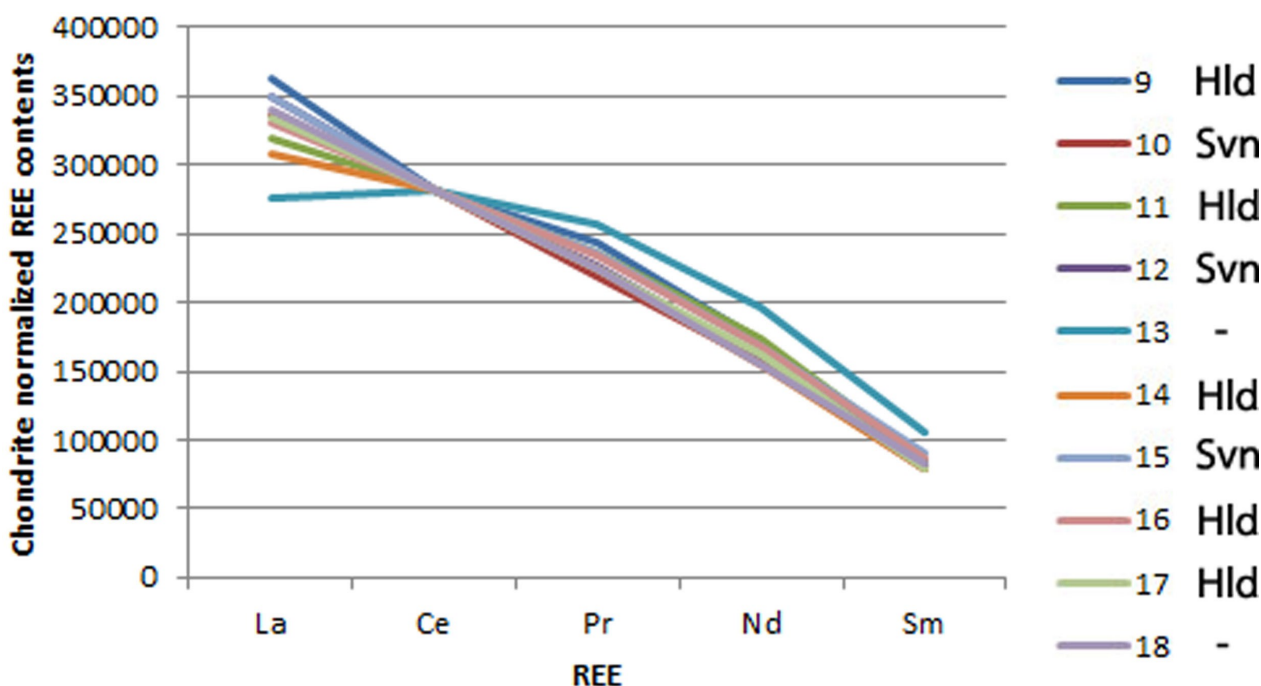
Fig. 19. Spider diagram showing only the LREE section of chondrite normalised REE contents in monazite from Stensjöstrand presented in Figure 14. Note that this plot does not have a logarithmic y-axis. Hld = Hallandian generation. Svn = Sveconorwegian generation. Points of unknown generation are marked with a dash (-).

9   Acknowledgements

10   References

Aleinikoff, J. N., Schenck, W. S., Plank, M. O., Srogi, L., Fanning, C. M., Kamo, S. L. & Bosbyshell, H., 2006: Deciphering igneous and metamorphic events in high-grade rocks of the Wilmington complex, Delaware: Morphology, cathodoluminescence and backscattered electron zoning, and SHRIMP U-Pb geochronology of zircon and monazite. *Bulletin of the Geological Society of America 118*, 39-64.

Andersson, J., Möller, C. & Johansson, L., 2002: Zircon geochronology of migmatite gneisses along the Mylonite Zone (S Sweden): A major Sveconorwegian terrane boundary in the Baltic Shield. *Precambrian Research 114*, 121-147.

Andersson, J., Söderlund, U., Cornell, D., Johansson, L. & Möller, C., 1999: Sveconorwegian (-Grenvillian) deformation, metamorphism and leucosome formation in SW Sweden, SW Baltic Shield: Constraints from a Mesoproterozoic granite intrusion. *Precambrian Research 98*, 151-171.

Beall, G. W., Boatner, L. A., Mullica, D. F. & Wo, W. O. M., 1981: The structure of cerium orthophosphate, a synthetic analogue of monazite. *Journal of Inorganic and Nuclear Chemistry 43*, 101-105.

Bingen, B., Demaiffe, D. & Hertogen, J., 1996: Redistribution of rare earth elements, thorium, and uranium over accessory minerals in the course of amphibolite to granulite facies metamorphism: The role of apatite and monazite in orthogneisses from southwestern Norway. *Geochimica et Cosmochimica Acta 60*, 1341-1354.

Bingen, B., Nordgulen, O. & Viola, G., 2008: A four-phase model for the sveconorwegian orogeny, SW Scandinavia. *Norsk Geologisk Tidsskrift 88*, 43-72.

Bingen, B., Skar, O., Marker, M., Sigmond, E. M. O., Nordgulen, O., Ragnhildstveit, J., Mansfeld, J., Tucker, R. D. & Liegeois, J.-P., 2005: Timing of continental building in the Sveconorwegian orogen, SW Scandinavia. *Norsk Geologisk Tidsskrift 85*, 87-105.

Bowring, S. A., Schoene, B., Crowley, J. L., Ramezani, J. & Condon, D. J., 2006: *High-precision U -Pb Zircon Geochronology and the Stratigraphic Record: Progress and Promise.*

Brander, L., Appelquist, K., Cornell, D. & Andersson, U. B., 2012: Igneous and metamorphic geochronologic evolution of granitoids in the central Eastern Segment, southern Sweden. *International Geology Review 54*, 509-546.

Buick, I. S., Clark, C., Rubatto, D., Hermann, J., Pandit, M. & Hand, M., 2010: Constraints on the Proterozoic evolution of the Aravalli-Delhi orogenic belt (NW India) from monazite geochronology and mineral trace element geochemistry. *Lithos (Oslo) 120*, 511-528.

Cherniak, D. J., Watson, E. B., Grove, M. & Harrison, T. M., 2004: Pb diffusion in monazite: A combined RBS/SIMS study. *Geochimica et Cosmochimica Acta 68*, 829-840.

Christoffel, C. A., Connelly, J. N. & Ahall, K.-I., 1999: Timing and characterization of recurrent pre-Sveconorwegian metamorphism and deformation in the Varberg-Halmstad region of SW Sweden. *Precambrian Research 98*, 173-195.

Coryell, C. D., Chase, J. W. & Winchester, J. W., 1963: A procedure for geochemical interpretation of terrestrial rare-earth abundance patterns. *Journal of Geophysical Research 68*, 559-566.

Faure, G. & Mensing, T. M., 2005: *Isotopes; principles and applications*. John Wiley & Sons, Hoboken, NJ, United States. 897 pp.

Fraser, G. L., Pattison, D. R. M. & Hearman, L. M., 2004: Age of Ballachulish and Glencoe Igneous Complexes (Scottish Highlands), and paragenesis of zircon, monazite and baddeleyite in the Ballachulish Aureole. *Journal of the Geological Society of London 161*, 447-462.

Gardes, E., Jaoul, O., Montel, J.-M., Seydoux-Guillaume, A.-M. & Wirth, R., 2006: Pb diffusion in monazite; an experimental study of Pb (super 2+) +Th (super 4+) --2Nd (super 3+) interdiffusion. *Geochimica et Cosmochimica Acta 70*, 2325-2336.

Gasquet, D., Bertrand, J.-M., Paquette, J.-L., Lehmann, J., Ratzov, G., De Ascencao Guedes, R., Tiepolo, M., Boullier, A.-M., Scaillet, S. & Nomade, S., 2010: Miocene to Messinian deformation and hydrothermal activity in a pre-Alpine basement

massif of the French Western Alps; new U-Th-Pb and argon ages from the Lauziere Massif. *Bulletin de la Societe Geologique de France 181*, 227-241.

Glitter. 2005. Glitter: Data Reduction Software for Laser Ablation Microprobe. Retrieved 10/28 2015, from http://www.glitter-gemoc.com/.

Günther, D. & Hattendorf, B., 2005: Solid sample analysis using laser ablation inductively coupled plasma mass spectrometry. *Trends in Analytical Chemistry 24*, 11.

Hafner, B., 2007: Scanning Electron Microscopy Primer. University of Minnesota Twin Cities, Characterization Facility. 29 pp.

Hansen, E., Johansson, L., Andersson, J., Labarge, L., Harlov, D., Möller, C. & Vincent, S., 2015: Partial melting in amphibolites in a deep section of the Sveconorwegian Orogen, SW Sweden. *Lithos 236-237*, 27-45.

Harley, S. K., Kelly, N. M. & Möller, A., 2007: Zircon behaviour and the thermal histories of mountain chains. *Elements*, 25-30.

Hassan, H. H., Hale, W. E. & Chrzanowski, M., 1988: *Geology of uranium and associated elements in New Brunswick*. Geological Survey of Canada, Calgary, AB, Canada. 82 pp.

Heier, K. S., 1979: The movement of uranium during higher grade metamorphic processes. *Philosophical Transactions of the Royal Society of London A (Mathematical and Physical Sciences) 291*, 413-421.

Högdahl, K., Majka, J., Sjostrom, H., Nilsson, K. P., Claesson, S. & Konecny, P., 2012: Reactive monazite and robust zircon growth in diatexites and leucogranites from a hot, slowly cooled orogen; implications for the Palaeoproterozoic tectonic evolution of the central Fennoscandian Shield, Sweden. *Contributions to Mineralogy and Petrology 163*, 167-188.

Horn, I., Rudnick, R. L. & Mcdonough, W. F., 2000: Precise elemental and isotope ratio determination by simultaneous solution nebulization and laser ablation-ICP-MS; application to U-Pb geochronology. *Chemical Geology 164*, 281-301.

Hoskin, P. W. O. & Schaltegger, U., 2003; The composition of zircon and igneous and metamorphic petrogenesis. *Reviews in Mineralogy and Geochemistry 53*, 27-62.

Hubbard, F. H., 1975: The Precambrian crystalline complex of south-western Sweden; the geology and

petrogenetic development of the Varberg region. *Geologiska Foreningens i Stockholm Forhandlingar 97*, Part 3, 223-236.

Hubbard, F. H., 1989: The geochemistry of Proterozoic lower-crustal depletion in Southwest Sweden. *Lithos 23*, 101-113.

Iolite. 2011. Iolite Software. Retrieved 10/28 2015, from http://iolite-software.com/.

Jackson, S., Dunning, G. R., Horn, I. & Longerich, H., 1997: The application of laser ablation microprobe (LAM)-ICP-MS to in situ zircon and monazite U-Pb geochronology. *Program with Abstracts - Geological Association of Canada; Mineralogical Association of Canada: Joint Annual Meeting 22*, 73.

Jakobsson, J., 2014: *The suitability of monazite and xenotime from Djupedal, south-eastern Sweden, as reference standards for U/Pb-dating with LA-ICP-MS*. University of Gothenburg. 44 pp.

Johansson, L., Lindh, A. & Möller, C., 1991: Late Sveconorwegian (Grenville) high-pressure granulite facies metamorphism in Southwest Sweden. *Journal of Metamorphic Geology 9*, 283-292.

Johansson, L., Möller, C. & Söderlund, U., 2001: Geochronology of eclogite facies metamorphism in the Sveconorwegian Province of SW Sweden. *Precambrian Research 106*, 261-275.

Kane, J. S., 1998: A history of the development and certification of NIST glass SRMs 610-617. *Geostandards Newsletter 22*, 7-13.

Kasapolu, B., Ersoy, Y. E., Uysal, I., Palmer, M. R., Zack, T., Koralay, E. O. & Karlsson, A., 2016: The petrology of Paleogene volcanism in the Central Sakaraya, Nallihan Region: Implications for the initiation and evolution of post-collisional, slab break-off-related magmatic activity. *Lithos 246-247*, 81-98.

Kelsey, D. E., Clark, C. & Hand, M., 2008: Thermobarometric modelling of zircon and monazite growth in melt-bearing systems: Examples using model metapelitic and metapsammitic granulites. 2 ed., Blackwell Publishing Inc. 199-212 pp.

Ketchum, J. W. F., Jackson, S. E., Culshaw, N. G. & Barr, S. M., 2001: Depositional and tectonic setting of the Paleoproterozoic Lower Aillik Group, Makkovik Province, Canada: Evolution of a passive margin-foredeep sequence based on petrochemistry and U-Pb (TIMS and LAM-ICP-MS) geochronology. *Precambrian Research 105*, 331-356.

Kosler, J. & Sylvester, P. J., 2003: Present trends and the future of zircon in geochronology; laser ablation

ICPMS. *Reviews in Mineralogy and Geochemistry 53*, 243-275.

Kundsen, T. L., Griffin, W. L., Hartz, E. H., Andresen, A. & Jackson, S. E., 2001: In-situ hafnium and lead isotope analyses of detrital zircons from the Devonian sedimentary basin of NE Greenland; a record of repeated crustal reworking. *Contributions to Mineralogy and Petrology 141*, 83-94.

Länsstyrelsen, H. L. 2015. Länsstyrelsen, Hallands Län. Retrieved 17/12 2015, from http://www.lansstyrelsen.se/halland/Sv/Pages/default.aspx.

Longerich, H. P. & Diegor, W., 2001: Introduction to mass spectrometry. *Short Course Handbook 29*, 1-19.

Ludwig, K. R., 1998: On the treatment of concordant uranium-lead ages. Geochimica *et Cosmochimica Acta 62*, 665-676.

Ludwig, K. R., 2012: Isoplot: A Geochronological Toolkit for Microsoft Excel. Berkeley, California, Berkeley Geochronology Center. 75 pp.

Machado, N., Gapais, D., Potrel, A., Gauthier, G. & Hallot, E., 2011: Chronology of transpression, magmatism, and sedimentation in the Thompson nickel belt (Manitoba, Canada) and timing of Trans-Hudson Orogen-Superior Province collison. *Canadian Journal of Earth Sciences = Revue Canadienne des Sciences de la Terre 48*, 295-324.

Mark Harrison, T., Ryerson, F. J., Le Fort, P., Yin, A., Lovera, O. M. & Catlos, E. J., 1997: A Late Miocene-Pliocene origin for the Central Himalayan inverted metamorphism. *Earth and Planetary Science Letters 146*, E1-E7.

Masuda, A., 1962: Regularities in variation of relative abundances of lanthanide elements and an attempt to analyse separation-index patterns of some minerals. *The Journal of Earth Sciences 20*, 173-187.

Mcfarlane, C. R. M., Connelly, J. N. & Carlson, W. D., 2006: Contrasting response of monazite and zircon to a high-T thermal overprint. *Lithos 88*, 135-149.

Möller, C., 1998: Decompressed eclogites in the Sveconorwegian (-Grenvillian) orogen of SW Sweden: petrology and tectonic implications. Journal *of Metamorphic Geology 16*, 641-656.

Möller, C., 1999: Sapphirine in SW Sweden; a record of Sveconorwegian (-Grenvillian) late-orogenic tectonic exhumation. *Journal of Metamorphic Geology 17*, 127-141.

Möller, C., Andersson, J., Dyck, B. & Antal Lundin, I., 2015: Exhumation of an eclogite terrane as a hot migmatitic nappe, Sveconorwegian orogen. *Lithos (Oslo) 226*, 147-168.

Möller, C., Andersson, J., Lundqvist, I. & Hellstrom, F., 2007: Linking deformation, migmatite formation and zircon U-Pb geochronology in polymetamorphic orthogneisses, Sveconorwegian Province, Sweden. *Journal of Metamorphic Geology 25*, 727-750.

Müller, A., Van Den Kerkhof, A. M., Behr, H.-J, Kronz, A. & Koch-Müller, M., 2010: The evolution of late-Hercynian granites and rhyolites documented by quartz, a review. *Special Paper-Geological Society of America 472*, 185-204.

Olsson, A., 2013: *Monazite in metasediments from Stensjöstrand: A pilot study*. Lund University. 13 pp.

Overstreet, W. C., 1967: *The geologic occurrence of monazite*. U. S. Geological Survey, Reston, VA, United States. 327 pp.

Paton, C., Woodhead, J. D., Hellstrom, J. C., Hergt, J. M., Greig, A. & Maas, R., 2010: Improved laser ablation U-Pb zircon geochronology through robust downhole fractionation correction. *Geochemistry, Geophysics, Geosystems - G (super 3) 11*.

Percival, J. A., Whalen, J. B. & Rayner, N., 2004: Pikwitonei-Snow Lake, Manitoba transect (parts of NTS 63J, 63O and 63P), Trans-Hudson Orogen-Superior Margin Metallotect Project; initial geological, isotopic and SHRIMP U-Pb results. *Report of Activities (Manitoba. Geological Survey)*, 120-134.

Percival, J. A., Whalen, J. B. & Rayner, N., 2005: Pikwitonei-Snow Lake Manitoba transect (parts of NTS 63J, 63O and 63P), Trans-Hudson Orogen-Superior Margin Metallotect Project; new results and tectonic interpretation. *Report of Activities (Manitoba. Geological Survey) 2005*, 69-91.

Petersson, A., Schersten, A., Andersson, J. & Möller, C., 2013: Zircon U-Pb and Hf-isotopes from the eastern part of the Sveconorwegian Orogen, SW Sweden; implications for the growth of Fennoscandia. *Special Publication - Geological Society of London 389*, 281-303.

Piñán-Llamas, A., Andersson, J., Möller, C., Johansson, L. & Hansen, E., 2015: Polyphasal foreland-vergent deformation in a deep section of the 1Ga Sveconorwegian orogen. Precambrian *Research 265*, 121-149.

31

Primer, 2005: Inductively Coupled Plasma Mass Spectrometry, a Primer. USA, Agilent Technologies. 84 pp.

Rayner, N., Zwanzig, H. V. & Percival, J. A., 2006: Detrital zircon provenance of the Pipe Formation, Ospwagan Group, Thompson nickel belt, Manitoba, NTS 63O8. *Report of Activities (Manitoba. Geological Survey) 2006*, 116-124.

Richter, M., 2013: *Evaluation of U-Th-Pb dating of monazite by LA-ICP-MS*. Mainz, Johannes Gutenberg-Universität. 191 pp.

Rollinson, H. R., 1993: *Using geochemical data; evaluation, presentation, interpretation*. Longman Scientific & Technical, Harlow, United Kingdom. 352 pp.

Rubatto, D., Williams, S. I. & Buick, S. I., 2001: Zircon and monazite response to prograde metamorphism in the Reynolds Range, central Australia. *Contributions to Mineralogy and Petrology 140*, 458-468.

Schoene, B. 2013: U-Th-Pb Geochronology. In H. H. a. K. Turekian (ed.): *Treatise on Geochemistry*, 2nd ed, 341-378. Elsevier Ltd.

Seydoux-Guillaume, A.-M., Paquette, J.-L., Wiedenbeck, M., Montel, J.-M. & Heinrich, W., 2002: Experimental resetting of the U-Th-Pb systems in monazite. *Chemical Geology 191*, 165-181.

Seydoux-Guillaume, A.-M., Wirth, R., Deutsch, A. & Scharer, U., 2004: Microstructure of 24-1928 Ma concordant monazites; implications for geochronology and nuclear waste deposits. *Geochimica et Cosmochimica Acta 68*, 2517-2527.

Smith, H. A. & Barreiro, B., 1990: Monazite U-Pb dating of staurolite grade metamorphism in pelitic schists. *Contributions to Mineralogy and Petrology 105*, 602-615.

Söderlund, U., Möller, C., Andersson, J., Johansson, L. & Whitehouse, M., 2002: Zircon geochronology in polymetamorphic gneisses in the Sveconorwegian Orogen, SW Sweden; ion microprobe evidence for 1.46-1.42 and 0.98-0.96 Ga reworking. *Precambrian Research 113*, 193-225.

Spear, F. S. & Pyle, J. M., 2002: Apatite, monazite, and xenotime in metamorphic rocks. Reviews in Mineralogy and Geochemistry 48, 293-335.

Tera, F. & Wasserburg, G. J., 1972: U-Th-Pb systematics in three Apollo 14 basalts and the problem of initial Pb in lunar rocks. *Earth and Planetary Science Letters 14*, 281-304.

Tual, L., Piñán-Llamas, A. & Möller, C., 2015: High-temperature deformation in the basal shear zone of an eclogite-bearing fold nappe, Sveconorwegian orogen, Sweden. *Precambrian Research 265*, 104-120.

Ulmius, J., Andersson, J. & Möller, C., 2015: Hallandian 1.45Ga high-temperature metamorphism in Baltica: P-T evolution and SIMS U-Pb zircon ages of aluminous gneisses, SW Sweden. *Precambrian Research 265*, 10-39.

Viana, R. R., Manttari, I., Kunst, H. & Jordt-Evangelista, H., 2003: Age of pegmatites from eastern Brazil and implications of mica intergrowths on cooling rates and age calculations. *Journal of South American Earth Sciences 16*, 493-501.

Wahlgren, C.-H., Cruden, A. R. & Stephens, M. B., 1994: Kinematics of a major fan-like structure in the eastern part of the Sveconorwegian Orogen, Baltic Shield, south-central Sweden. *Precambrian Research 70*, 67-91.

Wang, X.-D. & Lindh, A., 1996: Temperature-pressure investigation of the southern part of the southwest Swedish granulite region. *European Journal of Mineralogy 8*, 51-67.

Wang, X. D., Söderlund, U., Lindh, A. & Johansson, L., 1998: U–Pb and Sm–Nd dating of high-pressure granulite- and upper amphibolite facies rocks from SW Sweden. *Precambrian Research 92*, 319-339.

Wetherill, G. W., 1963: Discordant uranium-lead ages; [Part] 2, Discordant ages resulting from diffusion of lead and uranium. *Journal of Geophysical Research 68*, 2957-2965.

Wetherill, G. W., 1973: Discordant Uranium-Lead Ages, I [with comments]. *Geochronology; Radiometric Dating of Rocks and Minerals*. Dowden, Hutchinson & Ross; Benchmark Papers in Geology. 171-177 pp.

White, R. W., Powell, R. & Clarke, G. L., 2002: The interpretation of reaction textures in Fe-rich metapelitic granulites of the Musgrave Block, central Australia; constraints from mineral equilibria calculations in the system K (sub 2) O-FeO-MgO-Al (sub 2) O (sub 3) -SiO (sub 2) -H (sub 2) O-TiO (sub 2) -Fe (sub 2) O (sub 3). *Journal of Metamorphic Geology 20*, 41-55.

Williams, I. S., Buick, I. S. & Cartwright, I., 1996: An extended episode of early Mesoproterozoic metamorphic fluid flow in the Reynolds Range, central Australia. *Journal of Metamorphic Geology 14,* 29-47.

Williams, M. L., Jercinovic, M. J. & Hetherington, C. J., 2007: Microprobe monazite geochronology: Understanding geologic processes by integrating composition and chronology. *Annual Review of Earth and Planetary Sciences 35*, 137-175.

Wing, B. A., Ferry, J. M. & Harrison, T. M., 2003: Prograde destruction and formation of monazite and allanite during contact and regional metamorphism of pelites: petrology and geochronology. *Contributions to Mineralogy and Petrology 145*, 228-250.

Zeh, A., Williams, I. S., Braetz, H. & Millar, I. L., 2003: Different age response of zircon and monazite during the tectono-metamorphic evolution of a high grade paragneiss from the Ruhla crystalline complex, central Germany. *Contributions to Mineralogy and Petrology 145*, 691-706.

Zhu, X. K. & O'nions, R. K., 1999: Monazite chemical composition; some implications for monazite geochronology. *Contributions to Mineralogy and Petrology 137*, 351-363.

Zwanzig, H. V. & White, D. J., 2002: Crustal architecture and evolution of collisional zones in Trans-Hudson Orogen, Manitoba; no easy answers. *Program with Abstracts - Geological Association of Canada; Mineralogical Association of Canada: Joint Annual Meeting 27*, 132.

Appendix

Table 1. LA-ICP-MS spot information and U-Th-Pb data table. Left-most columns present spot numbers along with associated monazite, domain, BSE colour scale, in-situ textural position of said monazite grain, and laser spot size. Central columns present approximate concentrations of U, Th and U/Th ratios with internal σ errors. Right-most columns present $^{207}Pb/^{235}U$, $^{206}Pb/^{238}U$, $^{206}Pb/^{207}Pb$, and $^{208}Pb/^{232}Th$ isotopic dates (reported in Ma) with internal σ errors and $(^{207}Pb/^{235}U)/(^{206}Pb/^{238}U)$ concordance. Values with extreme ages and errors are marked in italic.

Spot#	Monazite	Domain	BSE	Leuco/Meso	Spot Size	U (ppm)	±σ	Th (ppm)	±σ	U/Th	±σ	$^{207}Pb/^{235}U$	±σ	$^{206}Pb/^{238}U$	±σ	$^{207}Pb/^{206}Pb$	±σ	$^{208}Pb/^{232}Th$	±σ	Conc%
43	3cE3	Outer	Bright	Mesosome	10	1150	23	6.30E+04	1.50E+03	0.0211	0.0007	1458	17	1540	28	1335	29	1533	39	106
44	3cE3	Inner	Gray	Mesosome	10	2394	67	6.71E+04	2.00E+03	0.0411	0.0015	1012	17	1022	23	992	33	1122	34	101
45	3cE2	Inner	Gray	Mesosome	10	1490	170	6.27E+04	1.90E+03	0.0274	0.0031	1057	21	1097	28	991	39	1256	65	104
46	3cE2	Core	Bright	Mesosome	10	923	31	5.95E+04	1.20E+03	0.0176	0.0006	1489	14	1499	20	1478	24	1565	32	101
47	3cE2	Outer	Bright	Mesosome	10	455	9	7.04E+04	1.40E+03	0.0074	0.0002	1005	17	1019	19	960	55	1101	25	101
48	3cE2	Outer	Bright	Mesosome	10	1005	28	6.53E+04	1.70E+03	0.0177	0.0009	977	13	1008	16	910	32	1094	21	103
49	3cE2	Unzoned	Gray	Mesosome	10	2390	170	5.91E+04	3.50E+03	0.0458	0.0028	1002	27	1066	80	1041	58	1021	40	106
50	3cE4	Core	Bright	Mesosome	10	413	9	6.53E+04	1.70E+03	0.0072	0.0002	1442	22	1486	36	1392	39	1580	45	103
51	3cE4	Inner	Bright	Mesosome	10	1751	83	6.43E+04	1.70E+03	0.0309	0.0017	939	13	941	16	927	32	1057	33	100
58	3cK3	Inner	Gray	Mesosome	10	522	19	7.28E+04	1.50E+03	0.0080	0.0002	1510	14	1576	26	1401	27	1610	34	104
59	3cK3	Core	Bright	Mesosome	10	389	6	8.79E+04	2.00E+03	0.0049	0.0001	1426	16	1434	25	1404	37	1443	30	101
60	3bG1	Inner	Gray	Mesosome	10	377	7	7.38E+04	1.50E+03	0.0057	0.0001	1483	17	1545	25	1382	40	1610	28	104
61	3bG1	Inner	Bright	Mesosome	10	902	23	7.82E+04	1.40E+03	0.0127	0.0003	1435	14	1464	27	1390	25	1546	28	102
62	3bL2	Inner	Gray	Mesosome	10	2129	73	7.49E+04	3.10E+03	0.0315	0.0011	989	17	996	27	963	34	1111	38	101
63	3bL2	Inner	Bright	Mesosome	10	606	26	9.43E+04	3.30E+03	0.0071	0.0002	1445	28	1446	45	1426	52	1482	39	100
64	*20bC4*	*Inner*	*Bright*	*Mesosome*	*10*	*17*	*2*	*1.49E+05*	*2.10E+04*	*0.0002*	*0.0000*	*5030*	*650*	*8.50E+03*	*1.50E+03*	*4260*	*410*			
65	*20bC4*	*Inner*	*Bright*	*Mesosome*	*10*	*12*	*1*	*1.88E+05*	*8.00E+03*	*0.0001*	*0.0000*	*4160*	*250*	*3670*	*340*	*4480*	*170*			
66	*20bD1*	*Core*	*Gray*	*Leucosome*	*10*	*323*	*12*	*1.66E+05*	*5.70E+03*	*0.0019*	*0.0001*	*2590*	*380*	*1730*	*280*	*3360*	*370*			
67	*20bD1*	*Outer*	*Bright*	*Leucosome*	*10*	*16*	*1*	*1.28E+05*	*5.80E+03*	*0.0001*	*0.0000*	*1310*	*130*	*1072*	*67*	*1620*	*300*			
68	*20bD1*	*Outer*	*Bright*	*Leucosome*	*10*	*20*	*1*	*1.43E+05*	*6.90E+03*	*0.0001*	*0.0000*	*1272*	*72*	*1043*	*50*	*1620*	*200*			
75	*20bG1*	*Core*	*Bright*	*Mesosome*	*10*	*61*	*9*	*1.80E+05*	*6.40E+03*	*0.0003*	*0.0000*	*1570*	*140*	*1463*	*81*	*1850*	*230*			
76	*20bG1*	*Inner*	*Bright*	*Mesosome*	*10*	*230*	*6*	*2.87E+05*	*9.50E+03*	*0.0009*	*0.0000*	*1053*	*25*	*1049*	*24*	*1046*	*76*	*1036*	*25*	*100*
77	*20bG1*	*Outer*	*Gray*	*Mesosome*	*10*	*69*	*6*	*1.53E+05*	*8.40E+03*	*0.0005*	*0.0000*	*3474*	*94*	*2540*	*120*	*4258*	*66*			
78	*20bG1*	*Outer*	*Gray*	*Mesosome*	*10*	*57*	*3*	*1.03E+05*	*4.40E+03*	*0.0006*	*0.0000*	*2014*	*69*	*1372*	*46*	*2780*	*100*			
79	*20bG1*	*Inner*	*Gray*	*Mesosome*	*10*	*10*	*1*	*7.60E+04*	*5.10E+03*	*0.0001*	*0.0000*	*5616*	*70*	*7950*	*330*	*4897*	*43*			
80	*20bD3*	*Inner*	*Gray*	*Leucosome*	*10*	*9*	*1*	*1.56E+05*	*6.50E+03*	*0.0001*	*0.0000*	*2470*	*520*	*2180*	*690*	*3010*	*500*	*977*	*29*	*69*
81	*20bD3*	*Core*	*Bright*	*Leucosome*	*10*	*14*	*1*	*1.26E+05*	*5.90E+03*	*0.0001*	*0.0000*	*1410*	*160*	*1069*	*78*	*1830*	*310*	*986*	*31*	
82	*20bD3*	*Outer*	*Bright*	*Leucosome*	*10*	*6*	*0*	*7.98E+04*	*3.80E+03*	*0.0001*	*0.0000*	*2620*	*250*	*1860*	*330*	*3530*	*270*			
83	3cB3	Core	Gray	Mesosome	10	380	14	7.28E+04	2.80E+03	0.0056	0.0001	1121	21	1078	20	1191	46	1130	25	96
84	3cB3	Outer	Bright	Mesosome	10	424	15	8.70E+04	3.60E+03	0.0052	0.0001	1036	19	976	20	1147	48	1088	29	94
85	3cB3	Inner	Gray	Mesosome	10	381	12	8.45E+04	2.90E+03	0.0048	0.0001	984	17	935	19	1082	44	1050	25	95
86	3cB3	Inner	Bright	Mesosome	10	423	11	8.69E+04	3.90E+03	0.0052	0.0002	969	19	928	16	1053	49	1061	25	96
87	*3cC1*	*Core*	*Gray*	*Leucosome*	*10*	*1398*	*48*	*6.92E+04*	*2.50E+03*	*0.0213*	*0.0007*	*1483*	*44*	*1153*	*35*	*1971*	*66*	*1182*	*34*	*78*
88	3cK1	Core	Gray	Mesosome	10	1004	17	46820	830	0.0226	0.0005	1453	17	1490	25	1388	27	1619	30	103
89	*3cK1*	*Outer*	*Gray*	*Mesosome*	*10*	*830*	*140*	*3.26E+04*	*5.70E+03*	*0.0256*	*0.0011*	*1470*	*150*	*1070*	*66*	*2030*	*260*			
90	3cK1	Outer	Gray	Mesosome	10	984	46	7.02E+04	1.50E+03	0.0147	0.0006	941	17	919	21	990	47	1027	25	98
91	3cK1	Core	Gray	Mesosome	10	1094	18	47820	870	0.0240	0.0005	1389	13	1347	20	1442	24	1600	28	97
92	3cK1	Inner	Gray	Mesosome	10	786	26	7.08E+04	1.70E+03	0.0115	0.0004	971	19	941	21	1030	44	1103	31	97
99	3bL1	Core	Gray	Mesosome	10	217	5	4.83E+04	1.40E+03	0.0047	0.0001	1433	29	1484	46	1389	78	1597	54	104
100	3bL1	Outer	Gray	Mesosome	10	1607	56	6.40E+04	1.90E+03	0.0259	0.0006	961	18	962	22	966	41	1109	29	100
101	3bL1	Inner	Bright	Mesosome	10	554	17	6.76E+04	2.70E+03	0.0086	0.0005	1038	21	995	19	1107	50	1244	30	96
102	3bL1	Inner	Gray	Mesosome	10	384	39	5.72E+04	2.00E+03	0.0071	0.0009	1374	21	1322	23	1449	42	1578	41	96
103	3bL1	Inner	Gray	Mesosome	10	188	10	6.29E+04	2.30E+03	0.0031	0.0001	1447	29	1441	31	1436	57			100
104	3bM1	Core	Bright	Leucosome	10	499	16	6.99E+04	2.40E+03	0.0073	0.0002	1430	20	1432	24	1414	36			100
105	3bM1	Outer	Bright	Leucosome	10	1099	36	6.70E+04	2.30E+03	0.0168	0.0004	973	14	953	16	1005	41			98
106	3bM2	Core	Bright	Leucosome	10	280	8	5.80E+04	1.40E+03	0.0050	0.0002	1438	26	1424	24	1437	57	1606	43	99
107	3bM2	Outer	Gray	Leucosome	10	2500	140	6.91E+04	3.50E+03	0.0371	0.0013	971	20	984	31	986	30	1094	36	101
108	3bF2	Unzoned	Gray	Leucosome	10	1100	51	6.86E+04	3.70E+03	0.0165	0.0007	995	20	991	29	1000	46	1101	38	100
109	3bF2	Unzoned	Gray	Leucosome	10	1207	36	7.57E+04	2.40E+03	0.0163	0.0005	1000	16	1007	19	974	38	1097	31	101
110	3bF2	Unzoned	Gray	Leucosome	10	1242	58	7.17E+04	3.40E+03	0.0177	0.0005	965	15	955	27	1022	38	1073	25	99
111	3bF2	Unzoned	Gray	Leucosome	10	1216	65	7.36E+04	4.30E+03	0.0169	0.0005	966	19	972	32	989	53	1082	33	101
112	*3bC3*	*Unzoned*	*Gray*	*Leucosome*	*10*	*688*	*56*	*7.68E+04*	*3.00E+03*	*0.0086*	*0.0005*	*1445*	*26*	*1082*	*34*	*1910*	*42*			
113	3bC3	Unzoned	Gray	Leucosome	10	342	15	5.87E+04	1.80E+03	0.0060	0.0003	1435	22	1438	27	1422	38	1548	24	100
114	3bC3	Unzoned	Gray	Leucosome	10	539	23	5.58E+04	1.90E+03	0.0098	0.0004	1001	21	964	21	1068	46	1136	23	96
115	*3bC2*	*Core*	*Gray*	*Leucosome*	*10*	*1*	*1*	*65*	*56*	*0.0180*	*0.0110*	*3410*	*120*	*2660*	*710*	*3780*	*310*			
116	3bA1	Core	Gray	Leucosome	10	547	12	5.73E+04	1.30E+03	0.0097	0.0002	991	21	958	33	1092	70			97
117	3bD1	Inner	Gray	Leucosome	10	458	9	7.26E+04	2.10E+03	0.0064	0.0001	1482	14	1522	24	1412	36	1615	35	103
118	3bH1	Inner	Bright	Mesosome	10	2656	72	6.46E+04	1.10E+03	0.0417	0.0012	1014	9	1030	14	979	19	1134	19	102
125	3cE1	Inner	Bright	Mesosome	10	1331	38	6.61E+04	2.10E+03	0.0199	0.0004	1497	16	1542	27	1429	28	1699	35	103
126	3cE1	Outer	Gray	Mesosome	10	1640	110	6.74E+04	1.90E+03	0.0238	0.0014	971	20	969	24	981	35	1096	25	100
127	3cE1	Inner	Bright	Mesosome	10	1506	40	7.72E+04	2.70E+03	0.0192	0.0004	1400	12	1374	18	1440	22	1501	34	98
128	3cE1	Inner	Bright	Mesosome	10	1135	43	4.99E+04	2.00E+03	0.0224	0.0005	1368	17	1356	26	1380	28	1591	39	99
129	3cJ1	Inner	Gray	Mesosome	10	1217	24	6.20E+04	1.40E+03	0.0193	0.0004	1475	13	1520	21	1416	24	1686	28	103
130	3cJ1	Inner	Bright	Mesosome	10	525	11	6.32E+04	1.90E+03	0.0081	0.0002	1437	14	1453	21	1421	22	1627	28	101
131	3cJ1	Inner	Bright	Mesosome	10	346	11	9.11E+04	2.60E+03	0.0037	0.0002	1381	19	1431	80	1422	74	1334	49	104
132	3cJ1	Inner	Bright	Mesosome	10	881	76	6.52E+04	2.20E+03	0.0129	0.0007	1427	15	1404	23	1455	23	1587	30	98
133	3cJ1	Outer	Gray	Mesosome	10	1610	120	6.55E+04	2.60E+03	0.0234	0.0010	950	10	928	16	1001	28	1080	23	98
134	3cJ1	Outer	Gray	Mesosome	10	1800	130	6.53E+04	2.20E+03	0.0263	0.0013	971	10	957	16	1014	27	1101	19	99
135	3cJ1	Inner	Bright	Mesosome	10	246	10	7.12E+04	2.70E+03	0.0034	0.0001	1376	19	1292	27	1509	48	1544	43	94
136	3cJ1	Outer	Bright	Mesosome	10	962	16	46880	970	0.0200	0.0004	1357	17	1301	23	1448	30	1587	34	96
137	3cJ1	Inner	Bright	Mesosome	10	678	77	6.85E+04	2.20E+03	0.0094	0.0009	1370	19	1326	29	1436	35	1548	34	97
138	3cJ4	Core	Gray	Mesosome	10	494	13	5.83E+04	1.60E+03	0.0083	0.0002	1502	16	1531	26	1456	31	1643	37	102
139	3cJ4	Inner	Bright	Mesosome	10	469	16	6.74E+04	1.90E+03	0.0068	0.0003	1319	17	1297	23	1354	34	1492	36	98
140	3cJ6	Inner	Bright	Mesosome	10	1114	35	5.26E+04	2.00E+03	0.0206	0.0005	1400	13	1387	21	1439	20	1533	32	99
141	3cJ6	Inner	Bright	Mesosome	10	1152	31	5.33E+04	1.70E+03	0.0209	0.0005	1382	13	1331	19	1458	22	1518	30	96
142	3cJ6	Inner	Bright	Mesosome	10	1152	31	5.12E+04	1.40E+03	0.0215	0.0005	1360	12	1309	20	1447	20	1533	34	96
143	3cJ6	Inner	Gray	Mesosome	10	1152	34	5.45E+04	1.70E+03	0.0205	0.0004	1354	13	1284	22	1472	22	1486	24	95
144	3cJ6	Inner	Bright	Mesosome	10	876	34	7.82E+04	2.00E+03	0.0109	0.0004	996	19	942	25	1130	54	1141	40	95
145	3cJ6	Outer	Gray	Mesosome	10	1360	95	7.50E+04	3.20E+03	0.0173	0.0008	1041	17	976	24	1194	34	1187	40	94
164	3cE2	Core	Bright	Mesosome	5	467	18	8.19E+04	3.30E+03	0.0052	0.0003	1466	35	1466	41	1450	70	1548	54	100
165	3cE5	Unzoned	Bright	Mesosome	5	573	15	7.78E+04	3.50E+03	0.0069	0.0004	1001	30	988	25	995	95	1078	29	99
166	3cE1	Inner	Bright	Mesosome	5	1835	61	8.56E+04	3.20E+03	0.0191	0.0005	1421	17	1398	25	1424	39	1529	41	98
167	3cJ6	Outer	Gray	Mesosome	5	2080	120	9.81E+04	4.50E+03	0.0186	0.0008	1045	23	1025	25	1024	67	1164	44	98

34

Spot#	Monazite	Domain	BSE	Leuco/Meso	Spot Size	U (ppm)	±σ	Th (ppm)	±σ	U/Th	±σ	Age ± σ $^{207}Pb/^{235}U$	±σ	$^{206}Pb/^{238}U$	±σ	$^{207}Pb/^{206}Pb$	±σ	$^{208}Pb/^{232}Pb$	±σ	Conc%
168	3cJ6	Outer	Bright	Mesosome	5	2003	60	1.01E+05	4.30E+03	0.0179	0.0007	1042	22	987	25	1113	62	1214	40	95
169	3cJ6	Outer	Bright	Mesosome	5	3107	70	9.95E+04	3.70E+03	0.0283	0.0010	943	16	909	18	990	42	978	27	96
170	3cL1	Core	Bright	Mesosome	5	460	22	8.17E+04	3.70E+03	0.0050	0.0002	1411	67	1422	65	1290	160	1569	82	101
171	3cL1	Outer	Gray	Mesosome	5	916	33	8.92E+04	3.80E+03	0.0093	0.0003	1430	26	1430	32	1426	55	1565	47	100
172	3cF4	Core	Gray	Leucosome	5	1487	52	8.38E+04	3.00E+03	0.0159	0.0008	987	29	990	32	921	88	1086	40	100
173	3cF4	Outer	Bright	Leucosome	5	1038	38	1.05E+05	4.50E+03	0.0091	0.0004	980	25	950	28	965	85	1028	36	97
174	3cF4	Outer	Bright	Leucosome	5	1458	47	1.04E+05	4.30E+03	0.0127	0.0006	968	29	912	34	1060	84	1019	37	94
175	3cF4	Core	Gray	Leucosome	5	2380	120	1.03E+05	6.30E+03	0.0211	0.0008	981	25	941	33	1054	78	1069	44	96

Table 2. Measured U-Th-Pb isotope ratios with internal σ errors and error correlations. The same spots marked in italic in Appendix Table 1 are also marked in this table.

Spot #	Ratios±σ										
	^{207}Pb/^{235}U	±σ	^{206}Pb/^{238}U	±σ	Error Correlation	^{238}U/^{206}Pb	±σ	^{207}Pb/^{206}Pb	±σ	^{208}Pb/^{232}Th	±σ
43	3.215	0.073	0.2701	0.0056	0.74	3.702	0.077	0.0861	0.0013	0.0788	0.0021
44	1.714	0.045	0.1719	0.0043	0.75	5.817	0.146	0.0724	0.0011	0.0571	0.0018
45	1.839	0.058	0.1856	0.0051	0.44	5.388	0.148	0.0724	0.0014	0.0641	0.0034
46	3.334	0.060	0.2613	0.0042	0.78	3.827	0.062	0.0926	0.0012	0.0805	0.0017
47	1.697	0.044	0.1714	0.0035	0.37	5.834	0.119	0.0718	0.0019	0.0560	0.0013
48	1.623	0.034	0.1693	0.0029	0.67	5.907	0.101	0.0695	0.0011	0.0556	0.0011
49	1.685	0.071	0.1800	0.0150	0.45	5.556	0.463	0.0741	0.0021	0.0518	0.0021
50	3.150	0.090	0.2595	0.0072	0.62	3.854	0.107	0.0888	0.0018	0.0813	0.0024
51	1.524	0.032	0.1573	0.0028	0.65	6.357	0.113	0.0702	0.0011	0.0537	0.0017
58	3.421	0.065	0.2771	0.0051	0.72	3.609	0.066	0.0891	0.0013	0.0829	0.0018
59	3.073	0.067	0.2493	0.0048	0.50	4.011	0.077	0.0891	0.0018	0.0740	0.0016
60	3.289	0.065	0.2710	0.0049	0.38	3.690	0.067	0.0884	0.0018	0.0829	0.0015
61	3.117	0.056	0.2551	0.0053	0.51	3.920	0.081	0.0885	0.0012	0.0795	0.0015
62	1.653	0.045	0.1672	0.0049	0.81	5.981	0.175	0.0714	0.0012	0.0565	0.0020
63	3.160	0.110	0.2516	0.0089	0.72	3.975	0.141	0.0904	0.0025	0.0761	0.0021
64	*424*	*98*	*3.8400*	*0.8500*	*1.00*	*0.260*	*0.058*	*0.6410*	*0.0850*		
65	*74.0*	*9.7*	*0.7960*	*0.0890*	*0.95*	*1.256*	*0.140*	*0.6250*	*0.0490*		
66	*19.8*	*6.8*	*0.3170*	*0.0600*	*0.99*	*3.155*	*0.597*	*0.3500*	*0.0750*		
67	*3.13*	*0.67*	*0.1820*	*0.0120*	*0.48*	*5.495*	*0.362*	*0.1210*	*0.0190*		
68	*2.64*	*0.24*	*0.1763*	*0.0093*	*0.20*	*5.672*	*0.299*	*0.1110*	*0.0110*		
75	*5.0*	*1.5*	*0.2570*	*0.0170*	*0.87*	*3.891*	*0.257*	*0.1400*	*0.0250*		
76	*1.834*	*0.068*	*0.1768*	*0.0044*	*0.32*	*5.656*	*0.141*	*0.0752*	*0.0027*	*0.0526*	*0.0013*
77	*31.9*	*3.1*	*0.4880*	*0.0290*	*0.93*	*2.049*	*0.122*	*0.5150*	*0.0220*		
78	*6.50*	*0.52*	*0.2375*	*0.0090*	*0.60*	*4.211*	*0.160*	*0.2000*	*0.0130*		
79	*259*	*18*	*2.4900*	*0.1700*	*0.93*	*0.402*	*0.027*	*0.7710*	*0.0190*		
80	*3.460*	*0.78*	*0.1660*	*0.0180*	*0.03*	*6.024*	*0.653*	*0.1530*	*0.0380*	*0.0495*	*0.0015*
81	*4.1*	*1.1*	*0.1820*	*0.0150*	*0.77*	*5.495*	*0.453*	*0.1470*	*0.0280*	*0.0500*	*0.0016*
82	*25*	*12*	*0.3660*	*0.0860*	*0.74*	*2.732*	*0.642*	*0.3800*	*0.0810*		
83	2.029	0.062	0.1821	0.0038	0.64	5.491	0.115	0.0803	0.0019	0.0575	0.0013
84	1.782	0.052	0.1636	0.0035	0.59	6.112	0.131	0.0786	0.0019	0.0553	0.0015
85	1.642	0.045	0.1562	0.0034	0.61	6.402	0.139	0.0758	0.0016	0.0533	0.0013
86	1.605	0.048	0.1549	0.0028	0.51	6.456	0.117	0.0747	0.0018	0.0539	0.0013
87	*3.330*	*0.190*	*0.1959*	*0.0066*	*0.78*	*5.105*	*0.172*	*0.1216*	*0.0045*	*0.0602*	*0.0018*
88	3.193	0.070	0.2601	0.0049	0.78	3.845	0.072	0.0885	0.0012	0.0834	0.0016
89	*3.530*	*0.700*	*0.1810*	*0.0120*	*0.92*	*5.525*	*0.366*	*0.1340*	*0.0190*		
90	1.530	0.043	0.1532	0.0037	0.65	6.527	0.158	0.0725	0.0016	0.0521	0.0013
91	2.925	0.050	0.2325	0.0038	0.72	4.301	0.070	0.0910	0.0011	0.0824	0.0015
92	1.606	0.049	0.1573	0.0038	0.83	6.357	0.154	0.0739	0.0016	0.0561	0.0016
99	3.110	0.120	0.2590	0.0091	0.11	3.861	0.136	0.0889	0.0036	0.0822	0.0029
100	1.581	0.046	0.1611	0.0040	0.71	6.207	0.154	0.0712	0.0013	0.0564	0.0015
101	1.786	0.058	0.1670	0.0034	0.62	5.988	0.122	0.0768	0.0019	0.0635	0.0016
102	2.879	0.081	0.2277	0.0044	0.49	4.392	0.085	0.0909	0.0023	0.0812	0.0022
106	3.130	0.100	0.2474	0.0047	0.48	4.042	0.077	0.0911	0.0026	0.0827	0.0023
107	1.605	0.052	0.1650	0.0056	0.60	6.061	0.206	0.0721	0.0010	0.0556	0.0019
108	1.666	0.053	0.1663	0.0052	0.74	6.013	0.188	0.0727	0.0016	0.0560	0.0020
109	1.680	0.043	0.1692	0.0035	0.69	5.910	0.122	0.0715	0.0012	0.0558	0.0016
110	1.580	0.035	0.1599	0.0048	0.51	6.254	0.188	0.0735	0.0013	0.0545	0.0013
111	1.593	0.049	0.1628	0.0057	0.52	6.143	0.215	0.0724	0.0019	0.0550	0.0017
112	*3.160*	*0.110*	*0.1829*	*0.0063*	*0.76*	*5.467*	*0.188*	*0.1173*	*0.0027*		
113	3.125	0.088	0.2501	0.0054	0.69	3.998	0.086	0.0900	0.0017	0.0796	0.0013
114	1.689	0.056	0.1613	0.0038	0.68	6.200	0.146	0.0754	0.0017	0.0578	0.0012
117	3.300	0.064	0.2665	0.0047	0.47	3.752	0.066	0.0898	0.0017	0.0832	0.0019
118	1.716	0.025	0.1733	0.0026	0.61	5.770	0.087	0.0718	0.0007	0.0577	0.0010
125	3.380	0.069	0.2705	0.0054	0.72	3.697	0.074	0.0904	0.0013	0.0877	0.0019
126	1.609	0.051	0.1624	0.0042	0.78	6.158	0.159	0.0720	0.0012	0.0557	0.0013
127	2.964	0.045	0.2376	0.0036	0.68	4.209	0.064	0.0908	0.0010	0.0771	0.0018
128	2.851	0.063	0.2342	0.0050	0.77	4.270	0.091	0.0877	0.0012	0.0819	0.0021
129	3.281	0.056	0.2661	0.0041	0.60	3.758	0.058	0.0896	0.0012	0.0870	0.0015
130	3.128	0.058	0.2529	0.0041	0.64	3.954	0.064	0.0900	0.0010	0.0838	0.0015
131	2.899	0.073	0.2490	0.0160	0.13	4.016	0.258	0.0901	0.0034	0.0682	0.0026
132	3.084	0.059	0.2434	0.0044	0.83	4.108	0.074	0.0916	0.0011	0.0817	0.0016
133	1.547	0.025	0.1550	0.0028	0.70	6.452	0.117	0.0727	0.0010	0.0549	0.0012

Spot #	Ratios±σ				Error						
	$^{207}Pb/^{235}U$	±σ	$^{206}Pb/^{238}U$	±σ	Correlation	$^{238}U/^{206}Pb$	±σ	$^{207}Pb/^{206}Pb$	±σ	$^{208}Pb/^{232}Th$	±σ
134	1.604	0.027	0.1601	0.0030	0.57	6.246	0.117	0.0732	0.0009	0.0560	0.0010
135	2.889	0.075	0.2221	0.0051	0.44	4.502	0.103	0.0946	0.0024	0.0794	0.0023
136	2.812	0.065	0.2238	0.0044	0.71	4.468	0.088	0.0910	0.0015	0.0817	0.0018
137	2.843	0.068	0.2285	0.0056	0.73	4.376	0.107	0.0907	0.0017	0.0796	0.0018
138	3.401	0.067	0.2683	0.0050	0.64	3.727	0.069	0.0915	0.0014	0.0847	0.0020
139	2.657	0.057	0.2230	0.0044	0.69	4.484	0.088	0.0871	0.0015	0.0766	0.0019
140	2.977	0.052	0.2401	0.0041	0.59	4.165	0.071	0.0907	0.0010	0.0788	0.0017
141	2.907	0.049	0.2294	0.0036	0.75	4.359	0.068	0.0918	0.0010	0.0780	0.0016
142	2.821	0.046	0.2252	0.0039	0.73	4.440	0.077	0.0912	0.0010	0.0788	0.0018
143	2.803	0.051	0.2205	0.0042	0.74	4.535	0.086	0.0924	0.0010	0.0763	0.0013
144	1.672	0.050	0.1574	0.0045	0.64	6.353	0.182	0.0778	0.0021	0.0581	0.0021
145	1.794	0.049	0.1636	0.0044	0.73	6.112	0.164	0.0801	0.0014	0.0605	0.0021
164	3.250	0.140	0.2558	0.0080	0.54	3.909	0.122	0.0926	0.0034	0.0796	0.0029
165	1.705	0.078	0.1659	0.0046	0.30	6.028	0.167	0.0756	0.0035	0.0548	0.0015
166	3.061	0.071	0.2424	0.0048	0.50	4.125	0.082	0.0907	0.0018	0.0786	0.0022
167	1.810	0.064	0.1725	0.0046	0.51	5.797	0.155	0.0736	0.0022	0.0593	0.0023
168	1.793	0.057	0.1657	0.0045	0.53	6.035	0.164	0.0776	0.0024	0.0619	0.0021
169	1.534	0.039	0.1515	0.0031	0.60	6.601	0.135	0.0727	0.0015	0.0496	0.0014
170	3.000	0.240	0.2470	0.0130	0.40	4.049	0.213	0.0868	0.0071	0.0807	0.0044
171	3.130	0.110	0.2487	0.0062	0.54	4.021	0.100	0.0911	0.0027	0.0805	0.0025
172	1.661	0.078	0.1661	0.0058	0.36	6.020	0.210	0.0711	0.0031	0.0552	0.0021
173	1.628	0.062	0.1590	0.0051	0.37	6.289	0.202	0.0727	0.0031	0.0522	0.0019
174	1.610	0.076	0.1522	0.0061	0.41	6.570	0.263	0.0759	0.0032	0.0517	0.0019
175	1.640	0.066	0.1562	0.0056	0.51	6.402	0.230	0.0750	0.0030	0.0543	0.0023

Table 3. Y, Lu, Pb, and Th concentrations (ppm) converted from CPS. Spots with extreme deviant values are marked in italic.

Spot#	Y (ppm)	±σ	Lu (ppm)	±σ	^{206}Pb (ppm)	±σ	^{207}Pb (ppm)	±σ	^{208}Pb (ppm)	±σ	Th (ppm)	±σ
43	15790	490	24	1.5	4644	89	6830	150	2191	54	3.31E+04	1.10E+03
44	5140	180	5.57	0.41	3158	81	3990	120	839	19	16720	430
45	3.19E+04	3.20E+03	51.9	5.9	4250	240	5890	510	4730	570	6.38E+04	6.00E+03
46	18910	710	27.3	1.5	4588	79	7220	140	2638	66	3.80E+04	1.30E+03
47	2.50E+04	1.00E+03	8.6	1.1	3001	61	3653	94	4400	110	9.28E+04	2.30E+03
48	13790	640	5.88	0.58	2953	53	3489	78	1896	96	4.00E+04	2.00E+03
49	8530	670	4.17	0.85	2700	110	3470	190	646	27	14560	780
50	4.15E+04	2.50E+03	103.1	7.4	4370	110	6610	180	6120	280	8.85E+04	4.60E+03
51	11260	460	5.01	0.4	2818	49	3419	92	977	37	2.15E+04	1.00E+03
58	3.67E+04	1.20E+03	62.3	2.7	4984	89	7510	140	5910	120	8.33E+04	1.90E+03
58	4.52E+04	1.60E+03	71	4	4478	85	6720	140	8540	150	1.36E+05	3.30E+03
60	6.66E+04	2.30E+03	113.9	6.2	4811	73	7130	150	8190	120	1.17E+05	2.40E+03
61	22750	680	24	1.7	4494	61	6750	120	3520	87	5.23E+04	1.30E+03
62	7440	410	5.41	0.67	2997	83	3601	98	1004	31	21120	700
63	3.08E+04	1.50E+03	50.3	5.6	4530	160	6880	240	5990	200	9.35E+04	2.90E+03
76	*1.61E+05*	*6.30E+03*	*323*	*14*	*3243*	*80*	*4060*	*160*	*33530*	*870*	*7.50E+05*	*2.10E+04*
83	2.92E+04	1.10E+03	8	1.2	3382	70	4530	140	5670	140	1.16E+05	2.80E+03
84	25010	830	6.6	1.1	3053	66	3990	120	5800	140	1.23E+05	3.20E+03
85	27000	920	7.55	0.99	2898	60	3670	100	6120	110	1.34E+05	3.40E+03
86	23970	990	6.4	1	2883	53	3580	100	5670	150	1.23E+05	4.10E+03
88	16530	650	24.6	1.5	4877	86	7170	150	2011	38	28210	660
90	14240	590	5.66	0.77	2840	71	3409	98	1937	79	4.40E+04	2.10E+03
91	15260	510	21.8	1.2	4382	74	6610	120	1877	39	26450	570
92	17410	850	7.3	1.1	2928	75	3580	110	2611	94	5.49E+04	2.10E+03
99	1.05E+05	6.00E+03	172	13	4670	130	6850	280	9300	300	1.35E+05	4.20E+03
100	11620	410	5.07	0.66	2989	72	3530	100	1159	34	24160	550
101	2.70E+04	2.20E+03	24.9	4.6	3201	66	4080	130	4030	230	7.47E+04	4.00E+03
102	6.09E+04	7.40E+03	97	14	4368	85	6580	190	6770	650	1.00E+05	1.10E+04
103	*1.16E+05*	*5.90E+03*	*242*	*13*	*4750*	*130*	*7180*	*290*	*14160*	*590*	*2.01E+05*	*7.80E+03*
104	3.31E+04	1.20E+03	56.4	3.5	4730	97	7000	190	6040	140	8.48E+04	2.00E+03
105	6830	220	1.59	0.37	3027	58	3636	89	1759	45	36950	780
106	7.72E+04	3.80E+03	148.1	9.3	4733	94	7100	240	8910	290	1.27E+05	5.60E+03
107	6150	280	7.03	0.97	2988	97	3550	120	788	33	16810	630
108	8980	390	2.3	0.51	3109	90	3720	110	1790	47	3.79E+04	1.60E+03
109	9680	430	3.25	0.61	3214	68	3794	98	1819	56	3.82E+04	1.10E+03
110	8510	350	2.58	0.5	2937	61	3523	74	1622	33	35090	940
111	8160	420	2.7	0.56	2971	94	3530	100	1706	48	3.67E+04	1.10E+03
113	5.89E+04	4.20E+03	130	10	4800	100	7120	200	7480	430	1.08E+05	6.00E+03
114	2.38E+04	1.70E+03	38.5	3.9	3098	70	3810	120	3230	180	6.43E+04	2.80E+03
116	2.11E+04	1.00E+03	9	1.8	2949	70	3720	130	2931	94	6.34E+04	1.50E+03
117	4.33E+04	1.10E+03	74.4	3.7	5115	90	7510	150	6890	120	9.58E+04	1.90E+03
118	4100	190	4.35	0.48	3308	51	3893	61	732	26	14800	500
125	15650	530	23.4	1.5	5290	110	7790	170	2308	51	30340	650
126	11590	450	4.9	0.66	3137	99	3680	130	1263	99	2.63E+04	1.70E+03
127	13400	370	18.9	1.2	4628	77	6840	120	2077	36	31250	700
128	15530	740	21.2	1.6	4630	100	6640	150	1929	44	26840	570
129	15740	490	21.5	1.3	5186	79	7550	130	2342	39	31070	600
130	3.27E+04	1.20E+03	78.5	4.6	4946	82	7220	140	5360	110	7.38E+04	1.90E+03
131	4.93E+04	3.40E+03	32.5	7.9	4370	120	6380	180	9290	390	1.61E+05	7.00E+03
132	20690	960	41.1	3.8	4817	92	7160	140	3510	210	4.88E+04	2.50E+03

Spot#	Y (ppm)	±σ	Lu (ppm)	±σ	^{206}Pb (ppm)	±σ	^{207}Pb (ppm)	±σ	^{208}Pb (ppm)	±σ	Th (ppm)	±σ
133	9540	340	8.74	0.64	3049	60	3592	66	1273	71	2.64E+04	1.20E+03
134	9180	370	8.47	0.61	3135	61	3707	68	1169	74	2.38E+04	1.30E+03
135	5.93E+04	1.70E+03	83.3	5.6	4323	99	6650	180	12090	330	1.77E+05	4.40E+03
136	15980	460	22.6	1.6	4459	88	6580	150	2161	44	29850	670
137	3.37E+04	3.30E+03	47.1	6.8	4490	120	6550	170	4820	530	6.97E+04	7.20E+03
138	3.59E+04	1.30E+03	94.4	4.7	5340	100	7930	160	5340	110	7.18E+04	1.90E+03
139	3.15E+04	1.60E+03	22.9	2.1	4401	80	6170	130	6030	260	9.03E+04	3.90E+03
140	17820	710	25.5	1.2	4712	73	6900	130	1987	35	28890	680
141	17100	640	25.8	1.3	4577	73	6780	110	1943	36	28490	610
142	15470	490	24.3	1.4	4450	73	6550	100	1888	44	27570	640
143	17220	490	24.3	1.3	4366	80	6490	110	1940	42	28970	550
144	15680	690	20.1	2.3	3075	74	3850	100	2729	85	5.49E+04	1.90E+03
145	12730	620	18.7	1.9	3173	59	4120	100	1812	65	3.51E+04	1.70E+03
164	7.16E+04	4.60E+03	113	12	4870	160	7040	300	8950	460	1.28E+05	6.80E+03
165	2.26E+04	1.20E+03	6	1.5	3117	87	3700	170	4690	230	9.85E+04	5.30E+03
166	15450	660	19.1	2	4622	93	6670	160	2290	50	33150	900
167	12620	730	4.2	1.1	3370	87	3950	140	1799	79	3.43E+04	1.60E+03
168	11390	720	9.5	1.8	3196	89	3930	130	1945	69	3.56E+04	1.40E+03
169	9340	460	4.35	0.7	2904	58	3365	85	1000	30	22820	800
170	8.58E+04	8.90E+03	141	22	4900	250	6590	520	9250	470	1.26E+05	4.50E+03
171	3.07E+04	1.30E+03	82.1	5.9	4740	120	6910	240	4930	120	6.97E+04	2.40E+03
172	9260	610	2.8	1.1	3230	110	3670	170	1991	99	4.07E+04	2.20E+03
173	2.17E+04	1.30E+03	7.1	2	3134	98	3610	140	3280	110	7.06E+04	2.70E+03
174	15440	870	6.4	2	2908	91	3550	170	2346	94	5.05E+04	2.30E+03
175	6330	350	2.02	0.69	3060	100	3650	150	1475	59	3.05E+04	1.30E+03

Table 4. REE and trace element concentrations (ppm) normalised to chondrite.

| Sample	3c	3c	3c	3c	20b	3b	3b	3b	3b	3c
Spot#	9	10	11	12	13	14	15	16	17	18
Element										
Al	0.00007	0.00013	0	0.00025	0	0.0003	0	0	0.00056	0.00007
P	48.08	46.02	48.25	51.19	45.67	42.38	51.14	47.92	47.05	48.71
Ca	0.887	1.04	0.93	0.942	0.359	0.728	1.091	0.768	0.968	0.951
Y	10034	3788	8520	10205	15793	7065	7310	10468	7738	6913
La	362888	336115	319309	349595	276324	308828	348832	331079	333459	340138
Ce	280720	280720	280720	280720	280720	280720	280720	280720	280720	280720
Pr	243073	219193	236740	227219	256844	224084	235154	233966	223888	224457
Nd	171946	156203	172772	158402	197028	155486	167533	168620	162903	154050
Sm	80321	79455	84777	83022	104731	79609	89737	86452	78786	83308
Eu	8144	6091	5335	6313	8982	4802	11165	9689	9316	6079
Gd	39505	38023	44364	46064	59566	38200	47837	45332	38831	44695
Tb	22533	18659	23821	30242	35017	20580	25787	26311	19928	26146
Dy	16233	9853	15803	20103	25704	13106	16204	18332	13336	15892
Ho	10197	3818	9066	10327	16367	7879	8238	11181	8041	7275
Er	7003	1387	5486	4546	9973	4375	3956	7050	5181	2968
Tm	4449	460	2942	1759	5137	2378	1626	4275	3116	1034
Yb	2629	151	1571	620	2619	1194	626	2429	1780	377
Lu	1647	65	893	290	1460	703	316	1416	1077	167
^{206}Pb	194	99	172	329	4	127	406	162	324	230
Th	1277604	1294575	1416598	1394244	4216713	1452058	1330906	1305320	1330482	1236959
^{238}U	62887	49149	55883	163906	1888	43050	215059	53685	132620	115617
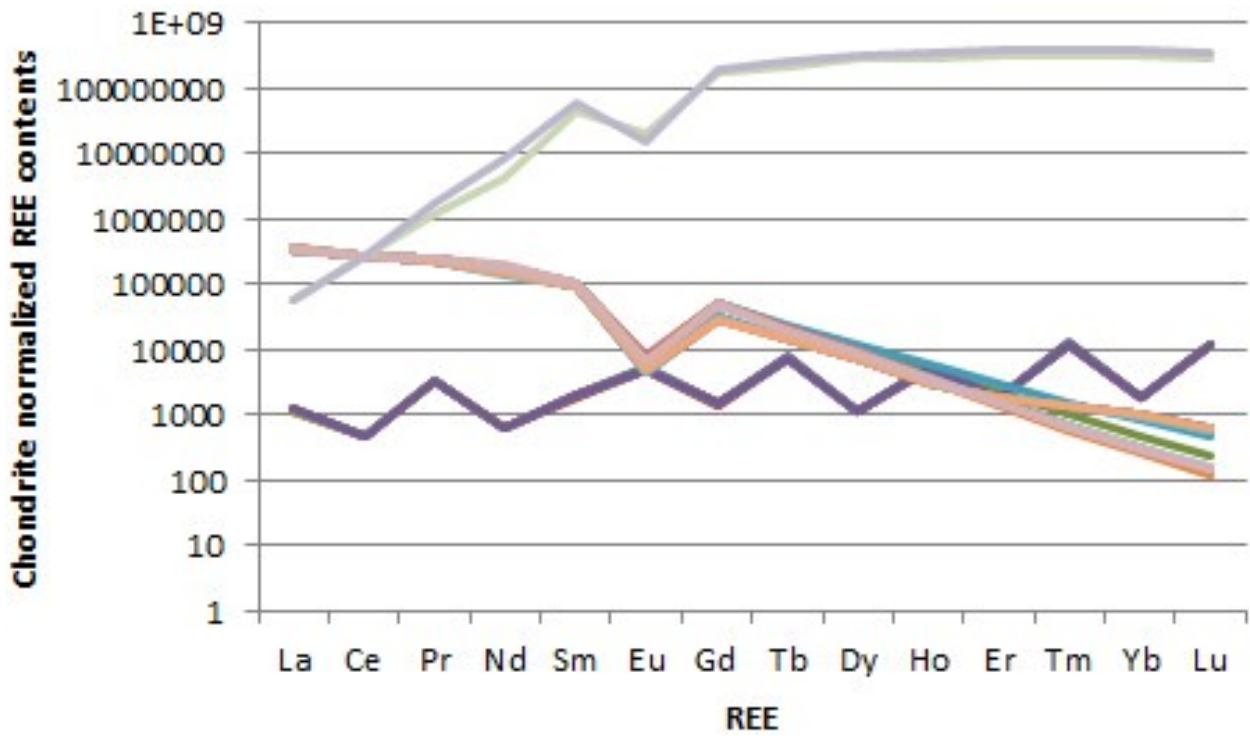
Fig. 1. Masuda-Coryell diagram (Masuda 1962; Coryell et al. 1963) showing chondrite normalised REE contents of standards Djupedal (xenotime top, monazite middle), Moacir (middle), and NIST SRM glass sample 610 (bottom).
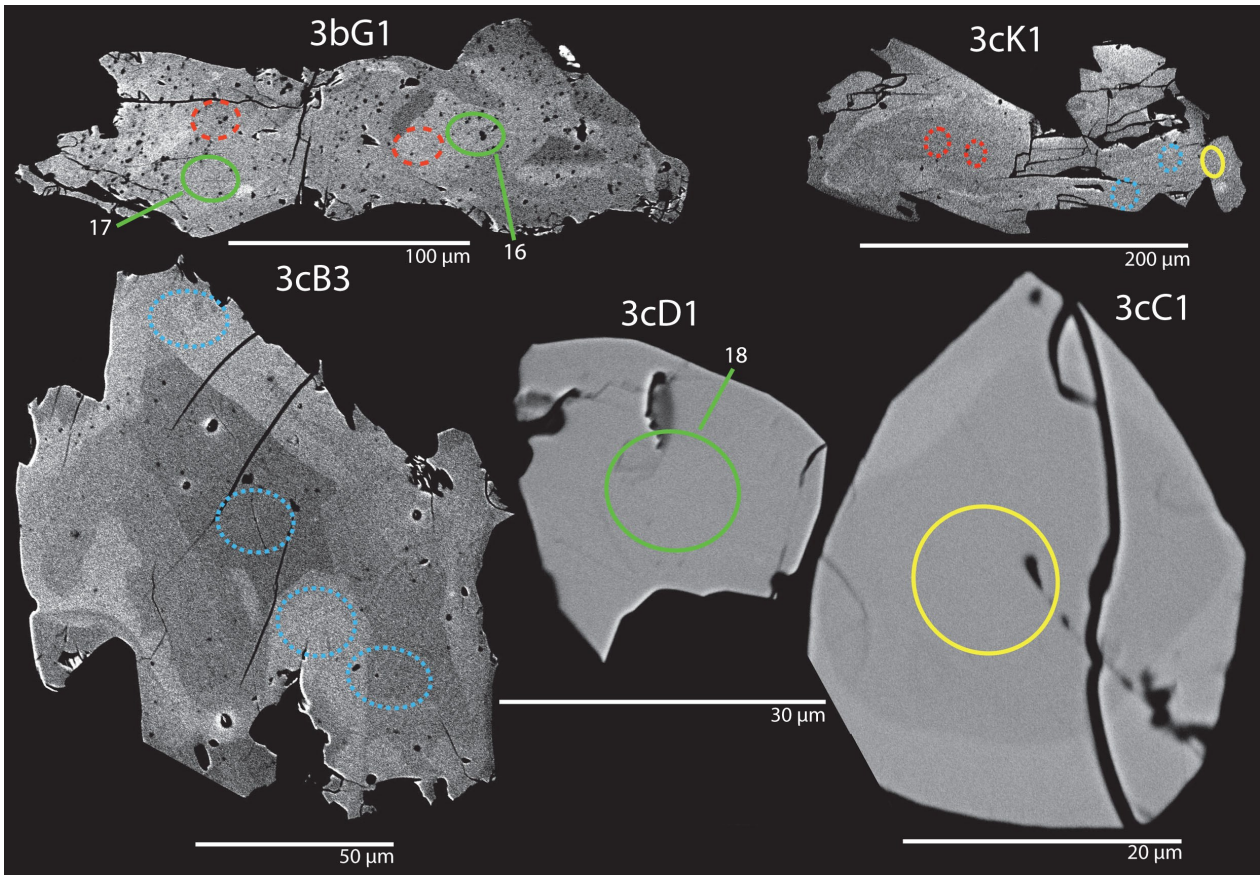
Fig. 2. BSE-images of monazite grains in mesosome with outlines of laser ablation pits, which were retrospectively traced over microscopy photographs. Overhead labels indicate the sample (09SGC-3b and -3c). These grains did not produce concordant data. Red and blue ellipses represent 1.43 Ga and 0.99 Ga generations respectively. Yellow ellipses represent rejected data points. Green ellipses represent REE analysis and are marked with spot numbers. Spot size is either 10 or 12 µm.
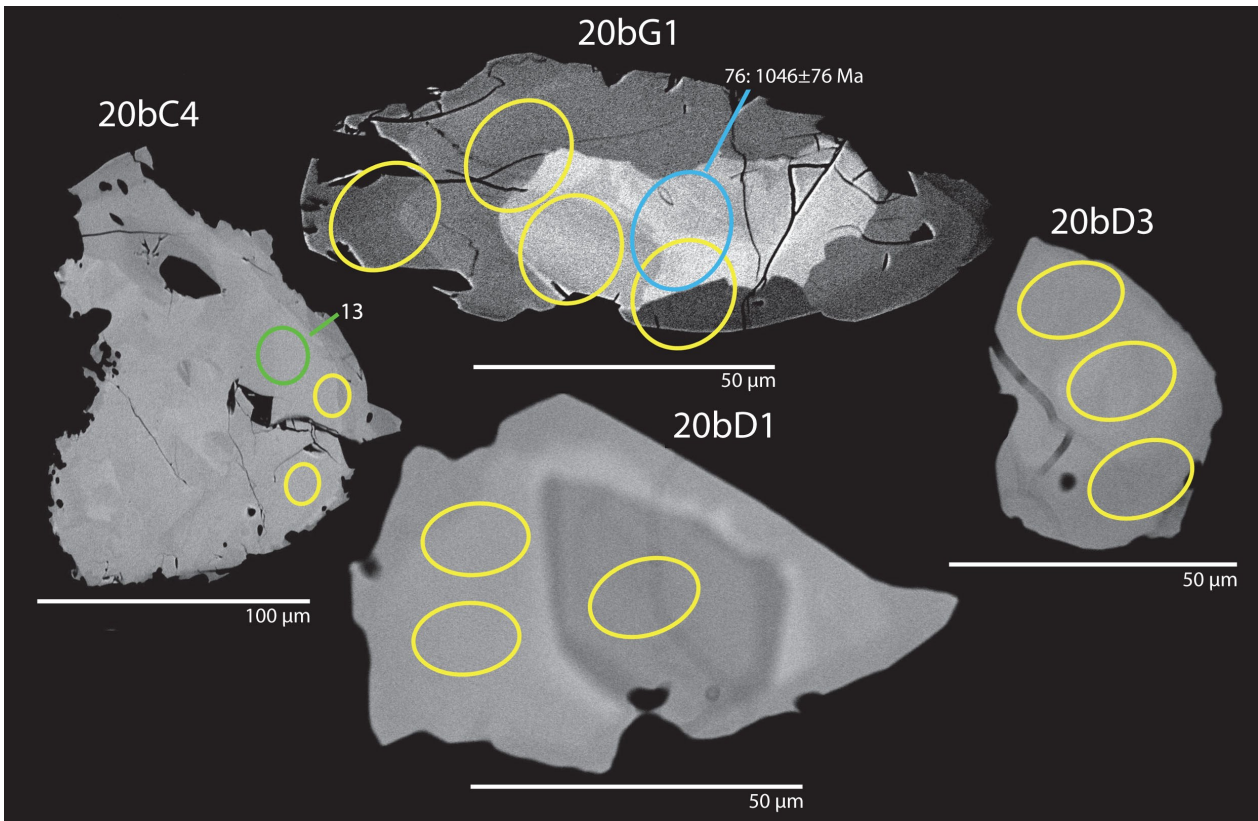
Fig. 3. BSE-images of analysed monazite grains from sample 09SGC-20b with outlines of laser ablation pits, which were retrospectively traced over microscope photographs. The blue ellipse represents a concordant $^{207}Pb/^{206}Pb$ isotopic date of the 0.99 generation. The yellow ellipses represent rejected points. The green ellipse represents REE analysis and is marked with spot number. Spot size is either 10 or 12 µm.

Tidigare skrifter i serien ”Examensarbeten i Geologi vid Lunds universitet”:

418. Mroczek, Robert, 2014: Microscopic shock-metamorphic features in crystalline bedrock: A comparison between shocked and unshocked granite from the Siljan impact structure. (15 hp)
419. Balija, Fisnik, 2014: Radon ett samhällsproblem - En litteraturstudie om geologiskt sammanhang, hälsoeffekter och möjliga lösningar. (15 hp)
420. Andersson, Sandra, 2014: Undersökning av kalciumkarbonatförekomsten i infiltrationsområdet i Sydvattens vattenverk, Vombverket. (15 hp)
421. Martin, Ellinor, 2014: Chrome spinel grains from the Komstad Limestone Formation, Killeröd, southern Sweden: A high-resolution study of an increased meteorite flux in the Middle Ordovician. (45 hp)
422. Gabrielsson, Johan, 2014: A study over Mg/Ca in benthic foraminifera sampled across a large salinity gradient. (45 hp)
423. Ingvaldson, Ola, 2015: Ansvarsutredningar av tre potentiellt förorenade fastigheter i Helsingborgs stad. (15 hp)
424. Robygd, Joakim, 2015: Geochemical and palaeomagnetic characteristics of a Swedish Holocene sediment sequence from Lake Storsjön, Jämtland. (45 hp)
425. Larsson, Måns, 2015: Geofysiska undersökningsmetoder för geoenergisystem. (15 hp)
426. Hertzman, Hanna, 2015: Pharmaceuticals in groundwater - a literature review. (15 hp)
427. Thulin Olander, Henric, 2015: A contribution to the knowledge of Fårö's hydrogeology. (45 hp)
428. Peterffy, Olof, 2015: Sedimentology and carbon isotope stratigraphy of Lower–Middle Ordovician successions of Slemmestad (Oslo-Asker, Norway) and Brunflo (Jämtland, Sweden). (45 hp)
429. Sjunnesson, Alexandra, 2015: Spårämnesförsök med nitrat för bedömning av spridning och uppehållstid vid återinfiltrationav grundvatten. (15 hp)
430. Henao, Victor, 2015: A palaeoenvironmental study of a peat sequence from Iles Kerguelen (49° S, Indian Ocean) for the Last Deglaciation based on pollen analysis. (45 hp)
431. Landgren, Susanne, 2015: Using calcein-filled osmotic pumps to study the calcification response of benthic foraminifera to induced hypoxia under *in situ* conditions: An experimental approach. (45 hp)
432. von Knorring, Robert, 2015: Undersökning av karstvittring inom Kristianstadsslättens NV randområde och bedömning av dess betydelse för grundvattnets sårbarhet. (30 hp)
433. Rezvani, Azadeh, 2015: Spectral Time Domain Induced Polarization - Factors Affecting Spectral Data Information Content and Applicability to Geological Characterization. (45 hp)
434. Vasilica, Alexander, 2015: Geofysisk karaktärisering av de ordoviciska kalkstensenheterna på södra Gotland. (15 hp)
435. Olsson, Sofia, 2015: Naturlig nedbrytning av klorerade lösningsmedel: en modellering i Biochlor baserat på en fallstudie. (15 hp)
436. Huitema, Moa, 2015: Inventering av föroreningar vid en brandövningsplats i Linköpings kommun. (15 hp)
437. Nordlander, Lina, 2015: Borrningsteknikens påverkan vid provtagning inför dimensionering av formationsfilter. (15 hp)
438. Fennvik, Erik, 2015: Resistivitet och IP-mätningar vid Äspö Hard Rock Laboratory. (15 hp)
439. Pettersson, Johan, 2015: Paleoekologisk undersökning av Triberga mosse, sydöstra Öland. (15 hp)
440. Larsson, Alfred, 2015: Mantelplymer - realitet eller *ad hoc*? (15 hp)
441. Holm, Julia, 2015: Markskador inom skogsbruket - jordartens betydelse (15 hp)
442. Åkesson, Sofia, 2015: The application of resistivity and IP-measurements as investigation tools at contaminated sites - A case study from Kv Renen 13, Varberg, SW Sweden. (45 hp)
443. Lönsjö, Emma, 2015: Utbredningen av PFOS i Sverige och världen med fokus på grundvattnet – en litteraturstudie. (15 hp)
444. Asani, Besnik, 2015: A geophysical study of a drumlin in the Åsnen area, Småland, south Sweden. (15 hp)
445. Ohlin, Jeanette, 2015: Riskanalys över pesticidförekomst i enskilda brunnar i Sjöbo kommun. (15 hp)
446. Stevic, Marijana, 2015: Identification and environmental interpretation of microtextures on quartz grains from aeolian sedi-

ments - Brattforsheden and Vittskövle, Sweden. (15 hp)

447. Johansson, Ida, 2015: Is there an influence of solar activity on the North Atlantic Oscillation? A literature study of the forcing factors behind the North Atlantic Oscillation. (15 hp)

448. Halling, Jenny, 2015: Inventering av sprickmineraliseringar i en del av Sorgenfrei-Tornquistzonen, Dalby stenbrott, Skåne. (15 hp)

449. Nordas, Johan, 2015: A palynological study across the Ordovician Kinnekulle. (15 hp)

450. Åhlén, Alexandra, 2015: Carbonatites at the Alnö complex, Sweden and along the East African Rift: a literature review. (15 hp)

451. Andersson, Klara, 2015: Undersökning av slugtestsmetodik. (15 hp)

452. Ivarsson, Filip, 2015: Hur bildades Bushveldkomplexet? (15 hp)

453. Glommé, Alexandra, 2015: $^{87}Sr/^{86}Sr$ in plagioclase, evidence for a crustal origin of the Hakefjorden Complex, SW Sweden. (45 hp)

454. Kullberg, Sara, 2015: Using Fe-Ti oxides and trace element analysis to determine crystallization sequence of an anorthosite-norite intrusion, Älgön SW Sweden. (45 hp)

455. Gustafsson, Jon, 2015: När började plattektoniken? Bevis för plattektoniska processer i geologisk tid. (15 hp)

456. Bergqvist, Martina, 2015: Kan Ölands grundvatten öka vid en uppdämning av de utgrävda dikena genom strandvallarna på Ölands östkust? (15 hp)

457. Larsson, Emilie, 2015: U-Pb baddeleyite dating of intrusions in the south-easternmost Kaapvaal Craton (South Africa): revealing multiple events of dyke emplacement. (45 hp)

458. Zaman, Patrik, 2015: LiDAR mapping of presumed rock-cored drumlins in the Lake Åsnen area, Småland, South Sweden. (15 hp)

459. Aguilera Pradenas, Ariam, 2015: The formation mechanisms of Polycrystalline diamonds: diamondites and carbonados. (15 hp)

460. Viehweger, Bernhard, 2015: Sources and effects of short-term environmental changes in Gullmar Fjord, Sweden, inferred from the composition of sedimentary organic matter. (45 hp)

461. Bokhari Friberg, Yasmin, 2015: The paleoceanography of Kattegat during the last deglaciation from benthic foraminiferal stable isotopes. (45 hp)

462. Lundberg, Frans, 2016: Cambrian stratigraphy and depositional dynamics based on the Tomten-1 drill core, Falbygden, Västergötland, Sweden. (45 hp)

463. Flindt, Anne-Cécile, 2016: A pre-LGM sandur deposit at Fiskarheden, NW Dalarna - sedimentology and glaciotectonic deformation. (45 hp)

464. Karlatou-Charalampopoulou, Artemis, 2016: Vegetation responses to Late Glacial climate shifts as reflected in a high resolution pollen record from Blekinge, south-eastern Sweden, compared with responses of other climate proxies. (45 hp)

465. Hajny, Casandra, 2016: Sedimentological study of the Jurassic and Cretaceous sequence in the Revinge-1 core, Scania. (45 hp)

466. Linders, Wictor, 2016: U-Pb geochronology and geochemistry of host rocks to the Bastnäs-type REE mineralization in the Riddarhyttan area, west central Berglsagen, Sweden. (45 hp)

467. Olsson, Andreas, 2016: Metamorphic record of monazite in aluminous migmatitic gneisses at Stensjöstrand, Sveconorwegian orogen. (45 hp)